EXPERIMENTAL INVESTIGATION OF THE EFFECTS OF ACOUSTIC WAVES ON NATURAL CONVECTION HEAT TRANSFER FROM A HORIZONTAL CYLINDER IN AIR

A Thesis

presented to

the Faculty of California Polytechnic State University,

San Luis Obispo

In Partial Fulfillment

of the Requirements for the Degree

Master of Science in Mechanical Engineering

by

Katherina Prodanov

March 2021

COMMITTEE MEMBERSHIP

TITLE:	Experimental Investigation of the Effects of Acoustic Waves on Natural Convection Heat Transfer from a Horizontal Cylinder in Air
AUTHOR:	Katherina Prodanov
DATE SUBMITTED:	March 2021
COMMITTEE CHAIR:	Glen Thorncroft, Ph.D. Professor of Mechanical Engineering
COMMITTEE MEMBER:	Richard Emberley, Ph.D. Assistant Professor of Mechanical Engineering
COMMITTEE MEMBER:	John Ridgely, Ph.D. Professor of Mechanical Engineering

ABSTRACT

Experimental Investigation of the Effects of Acoustic Waves on Natural Convection Heat Transfer from a Horizontal Cylinder in Air

Katherina Prodanov

Heat transfer is a critical part of engineering design, from the cooling of rocket engines to the thermal management of the increasingly dense packaging of electronic circuits. Even for the most fundamental modes of heat transfer, a topic of research is devoted to finding novel ways to improve it. In recent decades, investigators experimented with the idea of exposing systems to acoustic waves with the hope of enhancing thermal transfer at the surface of a body. Ultrasound has been applied with some success to systems undergoing nucleate boiling and in single-phase forced and free convection heat transfer in water. However, little research has been done into the use of sound waves to improve heat transfer in air.

In this thesis the impact of acoustic waves on natural convection heat transfer from a horizontal cylinder in air is explored. An experimental apparatus was constructed to measure natural convection from a heated horizontal cylinder. Verification tests were conducted to confirm that the heat transfer could be described using traditional free convection heat transfer theory. The design and verification testing of the apparatus is presented in this work. Using the apparatus, experiments were conducted to identify if the addition of acoustic waves affected the heat transfer. For the first set of experiments a 40 kHz standing wave was created along the length of the heated horizontal cylinder. While our expectation was that our results would mirror those found in the literature related to cooling enhancement using ultrasound in water (cited in the body of this thesis), they did not. When a 40 kHz signal was used to actuate the air surrounding the heated cylinder assembly, no measurable enhancement of heat transfer was detected. Experiments were also performed in the audible range using a loudspeaker at 200 Hz, 300 Hz, 400 Hz, 500 Hz, and 2,000 Hz. Interestingly, we found that a 200 Hz acoustic wave causes a significant, measurable impact on natural convection heat transfer in air from a horizontal cylinder. The steady state surface temperature of the cylinder dropped by approximately 12℃ when a 200 Hz wave was applied to the system.

Keywords: Natural Convection, Heat Transfer Enhancement, Acoustic Waves, Ultrasound

ACKNOWLEDGMENTS

I would like to thank all the people without whose support, guidance, and expertise this work would not be possible. Thanks to:

- Dr. Glen Thorncroft

  Thank you for being my thesis advisor. Your passion and excitement for helping your students grow and learn shines in your work. Throughout this thesis, I always felt as though you were in my corner with an optimistic perspective and constant support. From online learning due to COVID-19 to troubleshooting equipment, thank you for helping me brainstorm inventive ways to circumvent all the unexpected snags that popped up during this work. Above all, thank you for sharing your engineering knowledge and know-how with me; it made me a better engineer and helped me produce a thesis that I can be proud of.

- Dr. Richard Emberley and Dr. John Ridgely

  Thank you for being on my thesis committee. Your help with acquiring and troubleshooting temperature sensing equipment was vital to the success of this thesis. Thank you for answering my many questions and supporting this work.

- Cal Poly's Mechanical Engineering & Electrical Engineering Departments

  Thank you for loaning me the equipment necessary to complete this thesis.

- My Family

  Thank you for your unwavering support and love. I would not be where I am today without you. A special thanks to my father for helping me understand some of the finer points of electrical engineering which went into this thesis.

TABLE OF CONTENTS

LIST OF TABLES

Table Page

LIST OF FIGURES

Figure Page

LIST OF SYMBOLS

A_s	surface area
β	volumetric thermal expansion coefficient
C	constant in Morgan correlation
c_p	specific heat at constant pressure
c_s	speed of sound
D	diameter
dB	decibels
f	frequency
g	gravitational acceleration
Gr	Grashof number
γ	ratio of specific heats
h	heat transfer coefficient
Hz	Hertz
k	thermal conductivity
L	length
L_p	sound pressure level
λ	wavelength
M	molecular mass
μ	viscosity
n	constant in Morgan correlation
Nu	Nusselt number
p_o	reference sound pressure
Pr	Prandtl number
p_{rms}	root mean square sound pressure
Q	heat transfer rate
$q"$	heat flux
R	universal gas constant
Ra	Rayleigh number
ρ	density
T	temperature
T_s	surface temperature
T_∞	ambient temperature
V_{DC}	volts DC
V_{pp}	volts peak-to-peak
V_{rms}	volts root-mean-square
ν	kinematic viscosity
ξ	particle displacement

Chapter 1

INTRODUCTION

Heat transfer is a critical part of engineering design, from the cooling of rocket engines to the thermal management of the increasingly dense packaging of electronic circuits. As such, an ever-increasing number of innovative designs bring new challenges to optimizing heat transfer.

Heat transfer is not simply an applied science, however. Because of its complexity, much of the topic remains a subject of fundamental research. Boiling heat transfer, for example, is a complex combination of turbulent fluid motion combined with the growth and motion of vapor bubbles. There remains much to be understood and tested for models to emerge in the literature.

Even for the most fundamental (and best understood) modes of heat transfer, a topic of research is devoted to finding ways to improving heat transfer in novel ways. In recent decades, investigators experimented with the idea of exposing systems to sound waves in the hopes of enhancing the thermal transfer at the surface of a body. Ultrasound has been applied to systems undergoing nucleate boiling. The same has been done, with some success, in single-phase forced and free convection heat transfer in water. But there have been few attempts to study the impacts of acoustic waves on heat transfer in air.

In this work, the impact of acoustic waves is studied under conditions of natural convection in quiescent air. Natural convection was a deliberate choice: if sound waves could affect the fluid behavior in air, the effect of sound waves might likely be undetectable in comparison to any forced convection heat transfer.

An experimental investigation was undertaken to attempt to detect whether sound can augment natural convection in air. An experimental apparatus was constructed to measure natural convection from a heated horizontal cylinder. The design and verification testing of the apparatus is presented in this work. Experiments were then conducted to confirm that the heat transfer without the presence of acoustic waves could be described using traditional free convection heat transfer theory. Finally, sound waves were applied to the system to identify if the addition of acoustic actuation affected the heat transfer.

1.1 Literature Review

The impact of acoustic waves on heat transfer processes has been investigated for decades, with publications on the topic dating back nearly sixty years [1-3]. The research is largely experimental. Various groups have studied the effect of ultrasound in phase-change heat transfer [4, 5], heat exchangers [6, 7], and in both natural and forced convection regimes [8, 9].

Studies have shown that both the freezing and boiling of water can be affected by ultrasonic waves. In their experimental study of frost formation on a flat surface, Li et al. found that there was a visible difference in the freezing water droplets formed while the surrounding air was actuated with a 20 kHz ultrasonic wave and those formed in the absence of ultrasound [4]. The influence of ultrasonic waves can also be seen in Boziuk, Smith, and Glezer's work in enhanced boiling heat transfer. Their experimental measurements, with an acoustic actuation of 1.7 MHz, demonstrated a significant increase in the critical heat flux of water. With ultrasonic actuation, the critical heat flux for a plain surface saw a 66% improvement over that seen in non-actuated boiling [5].

Ultrasonic actuation has also been seen to affect heat transfer processes in heat exchangers. Monnot et al. found that ultrasound had a significant impact on the heat transfer between a cooling flow and a liquid inside a vessel. The study showed that the overall heat transfer coefficient of the cooling flow was enhanced the by up to 100% when in the presence of an ultrasonic field with frequencies ranging from 20 kHz to 1600 kHz. As such, the cooling rate of the system was increased [7].

Both forced and natural convection in water can be influenced by ultrasound for various heating element geometries. In their study of forced convection, Inworn and Chaiwaorapuek investigate the heat transfer capability between near-wall water and a heated flat surface under ultrasonic waves of various frequencies. They found that ultrasound decreases the temperature of the heated surface, resulting in an increase of the local Nusselt number. Furthermore, they saw that higher wave frequencies resulted in greater impacts on heat transfer. The Nusselt number increased by up to 10%, 16.5%, and 20.8%, at frequencies of 25, 33, and 40 kHz, respectively [8]. The experimental results for the 40 kHz case as compared to the control case (with no ultrasonic waves) can be seen in the authors' visualizations in Figure 1.1. The contours of RGB, hue signal value (H), surface temperature (T_s), and local Nusselt number (Nu_x) are plotted against the dimensionless spanwise distance (Y) in plots a, b, c, and d, respectively.

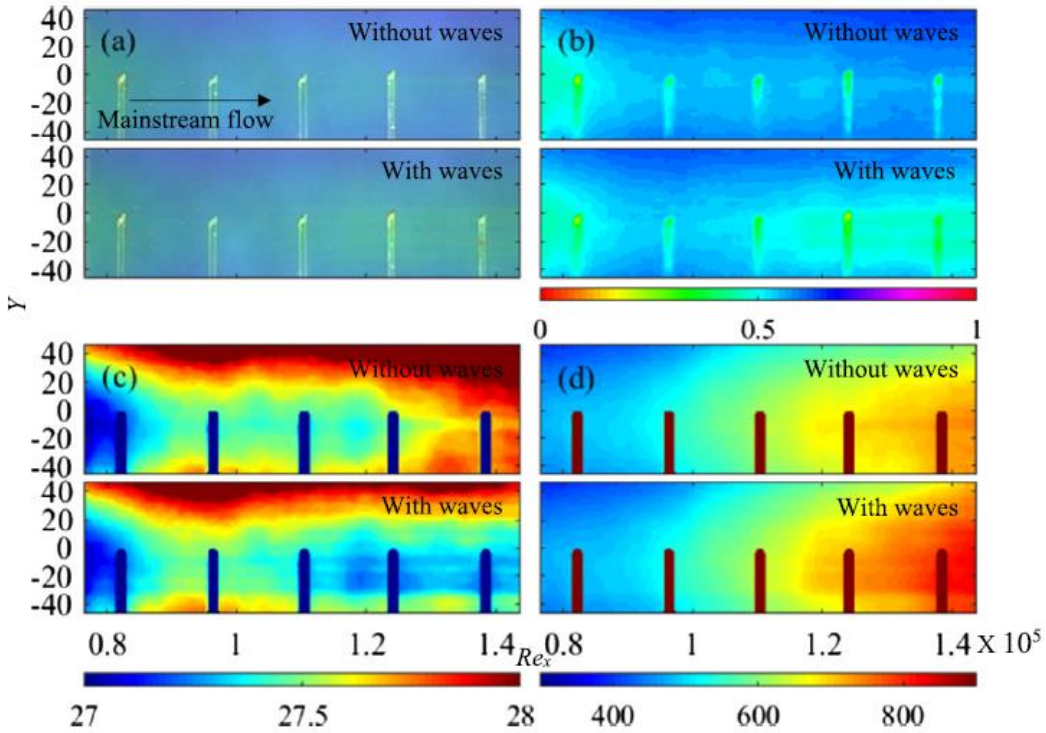

Figure 1.1. The contours of (a) RGB, (b) H, (c) T_s (℃), and (d)Nu_x signal under 40kHz ultrasonic waves. Reprinted from [8].

Inworn and Chaiwaorapuek concluded that the visualizations shown in Figure 1.1 further support their findings that ultrasonic waves have a measurable effect on heat transfer from a flat heating surface experiencing forced convection in water [8].

Baffigi and Bartoli had a similar conclusion in their investigation of the influence of ultrasound in single phase free convection in water. In this experiment, a hollow horizontal cylinder, heated via the Joule effect, was immersed in distilled water actuated by a 40 kHz acoustic wave. Under these conditions, the study found that the heat transfer coefficient (h) was enhanced by a 24% maximum with ultrasound [9]. A comparison of the recorded h values for with and without ultrasound can be seen in the authors' plot shown in Figure 1.2.

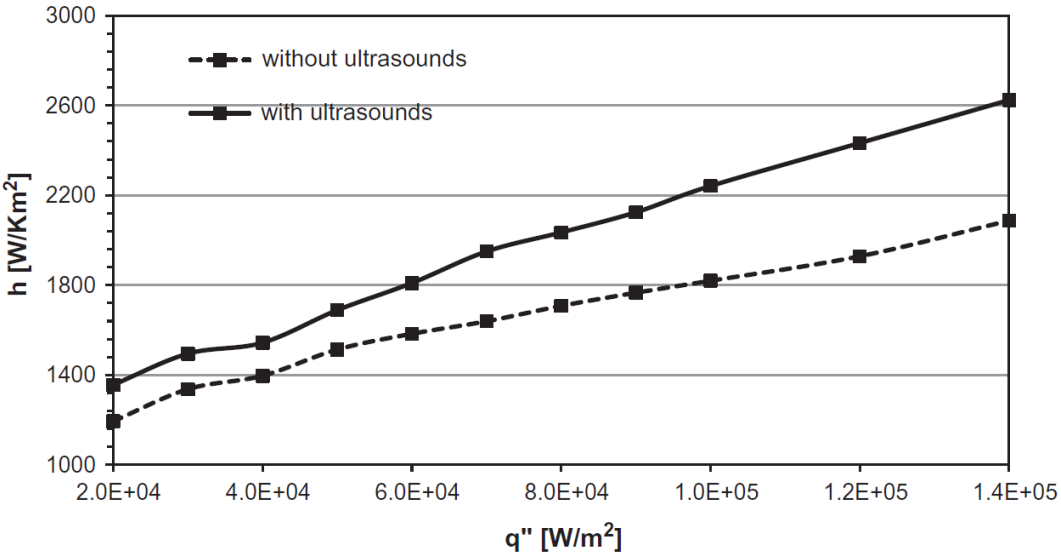

Figure 1.2. h vs $q^{"}$, at $T = 25℃$ (single phase conditions) without ultrasound, and with ultrasound, at f = 40 kHz. Reprinted from [9].

There is a relatively large number of works which further support the heat transfer altering effects of ultrasonic waves in liquid media. Leal et al. [10] summarize sixteen studies that investigate the use of ultrasound in a variety of heat transfer conditions. From these, that authors conclude that heat transfer in both boiling and non-boiling configurations can be impacted by ultrasonic actuation [10].

A single work examining the effect of sound on natural convection was found. In this study, Engelbrecht and Pretorius found that sound waves have an influence on the transition from laminar to turbulent flow in the boundary layer associated with natural convection from a vertical flat plate with uniform surface heat flux [11]. Although the investigators focused only on the hydrodynamic effects and did not examine heat transfer, their study lends credence to the idea that the heat transfer enhancement seen in liquid could also be replicated in air.

1.2 Thesis Objective and Scope

The objective of this thesis is to design and build an experimental apparatus to determine the effects of ultrasonic waves on natural convection heat transfer in air.

This document details the development, design, construction, and verification of the experimental apparatus used. Additionally, it describes the experimental methodologies and results for the investigation of the effects of ultrasonic waves on natural convective heat transfer in air. Chapter 2 presents the development of the experimental apparatus and the fundamental theories which underline critical design choices. An overview of the entire experimental system is presented in Chapter 3. The assembly and verification of the sensing, heating, and ultrasound subsystems are detailed in Chapters 4, 5, and 6, respectively. Chapter 7 describes the experiments performed with a 40 kHz signal and discusses the experimental results. Chapter 8 describes the experiments performed with a 200 kHz signal and discusses the experimental results. Finally, Chapter 9 concludes the work and presents recommendations for future work.

Chapter 2

EXPERIMENT CONCEPT AND THEORETICAL BASIS

This chapter discusses the conceptual design of the experiment and the fundamental theories relating to critical design choices.

2.1 Design Concept for Experiment

The design concept for this experiment features a heated, horizontal cylinder suspended in room-temperature air actuated by a standing 40 kHz acoustic wave. A diagram depicting the concept is shown in Figure 2.1.

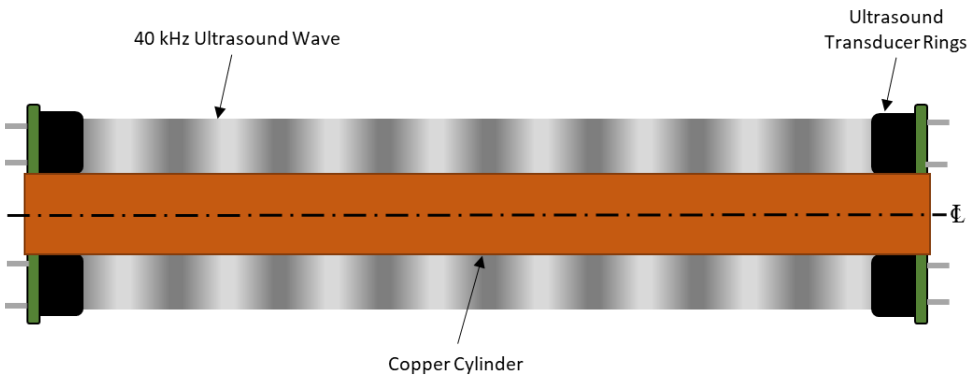

Figure 2.1. Cross sectional diagram of design concept for experiment.

The horizontal cylinder geometry was chosen for two reasons. First, the geometry is well-studied for both natural convection and cross flow conditions and is a classic "textbook problem" [12, 13]. This allowed us to verify portions of the experiment with trusted correlations. Second, as discussed in the Literature review presented in Section 1.1, Baffigi and Bartoli [9] found success using a hollow horizontal cylinder in their experiments. This gives us confidence that the geometry is appropriate for an investigation of ultrasound's effect on convection heat transfer.

Similarly, a 40 kHz ultrasonic wave frequency was selected for two reasons. First, there were several studies that successfully altered heat transfer processes using a 40 kHz signal [8, 9, 10]. Again, this gives us confidence that the frequency is appropriate for the experiment. Second, 40 kHz transducers are relatively easy to find and inexpensive, due to their use in other fields.

2.2 Natural Convection Theory

Steady state natural convection from a horizontal cylinder is a well-studied phenomenon. It is governed by the continuity equation, the 2-D Navier-Stokes equations, and the energy equation [14]. From these fundamental equations, dimensionless groups can be derived to characterize the natural convection heat transfer from an isothermal horizontal cylinder. From the derivations presented by Incropera and Dewitt [12], the following dimensionless numbers are determined:

The Prandtl number (Pr) is the ratio of the momentum and thermal diffusivities, and can be written in the following form:

$$Pr = \frac{\mu c_p}{k}, \tag{2.1}$$

where μ is the viscosity, c_p is the specific heat at constant pressure, and k is the thermal conductivity.

The Grashof number (Gr_D) is a measure of the ratio of buoyancy forces to viscous forces, and is written in the following form for a circular cylinder:

$$Gr_D = \frac{g\beta(T_s - T_\infty)D^3}{\nu^2}, \tag{2.2}$$

where g is the gravitational constant, β is the volumetric thermal expansion coefficient, v is the kinematic viscosity, D is the diameter of the cylinder, T_s is the temperature of the cylinder surface, and T_∞ is the ambient temperature.

The Rayleigh number characterizes the flow regime and is the product of the Grashof number and Prandtl number:

$$Ra = Gr\ Pr. \tag{2.3}$$

The Nusselt number (Nu_D) is particularly useful in characterizing boundary layer behavior. It is the ratio of convection to pure conduction heat transfer, and can be written in the following form for a circular cylinder:

$$Nu_D = \frac{hD}{k}, \tag{2.4}$$

where h is the convection heat transfer coefficient, D is the diameter of the cylinder, and k is the thermal conductivity of the fluid.

As h is often unknown or difficult to determine, experimental correlations for the Nusselt number have also been developed. Churchill and Chu [13] recommend the following correlation for the average Nusselt number over the entire circumference of a horizontal isothermal cylinder:

$$\overline{Nu_D} = \left\{0.60 + \frac{0.387Ra_D^{1/6}}{[1 + (0.559/Pr)^{9/16}]^{8/27}}\right\}^2. \tag{2.5}$$

This correlation applies to conditions where $Ra_D \leq 10^{12}$.

Another correlation for the average Nusselt number over the circumference of a horizontal isothermal cylinder is presented by Morgan [15]:

$$\overline{Nu_D} = C\, Ra_D{}^n, \tag{2.6}$$

where C and n are constants for free convection on a horizontal circular cylinder. For a Ra_D in the range of 10^4 through 10^7 $C = 0.480$ and $n = 0.250$ [15].

Newton's law of cooling, as described in [12] and show below, can also be used in natural convection conditions:

$$q" = h(T_s - T_\infty), \tag{2.7}$$

where $q"$ is the heat flux into the system. Using the Churchill and Chu, and Morgan correlations in conjunction with equations 2.1 – 2.4 and 2.7, we can later verify the experimental apparatus.

2.3 Sound Wave Theory

Acoustic (or sound) waves are longitudinal pressure waves which travel through a medium (like air or water). The speed of a sound wave depends on the type of medium it is traveling through and the state of that medium. The derivation of the equation for the speed of sound in air starts with the mass flow rate and continuity equations and can be found in Ling et al. [16]. Ultimately, the equation for the speed of sound (c_s) in gas media can be expressed in the following form:

$$c_s = \sqrt{\frac{\gamma RT}{M}}, \tag{2.8}$$

where γ is the ratio of specific heats, R is the universal gas constant, T is the absolute temperature, and M is the molecular mass.

The equation can be further simplified for the speed of sound in air assuming $\gamma = 1.4,\ R = 8.31\ \mathrm{J/mol}$, and $M = 0.02897\ \mathrm{kg/mol}$,

$$c_s \approx 331 \frac{m}{s} \sqrt{\frac{T}{273\ \mathrm{K}}}. \tag{2.9}$$

At room temperature ($T = 293$ K) the speed of sound is $c_s = 343\ \mathrm{m/s}$.

The speed of sound is related to the frequency (f) and wavelength (λ) of the sound wave in the following manner:

$$c_s = f\lambda. \tag{2.10}$$

It is important to note that the audible frequency range for humans is between 20 and 20,000 Hz. Frequencies below 20 Hz are considered subsonic, whereas frequencies above 20 kHz are considered ultrasonic. Our primary experiment will be conducted in the ultrasonic range at 40 kHz.

The audible loudness of a sound wave is related to the pressure of the wave. The higher the pressure of the wave, the higher the amplitude of the signal, the "louder" it is. To emit a high-pressure wave, powerful transducers are required. However, Dunst et al. [16] suggest that an alternative to using more powerful transducers is to increase the intensity of the acoustic wave by optimizing the boundary conditions of a standing wave field.

Ling et al. [18] define a standing wave as waves "that bounce back and forth through a particular region, effectively becoming stationary" [18]. Additionally, the authors provide the family of curves shown in Figure 2.2 to illustrate the phenomenon. Each curve represents the variation of pressure over space at a given instance in time.

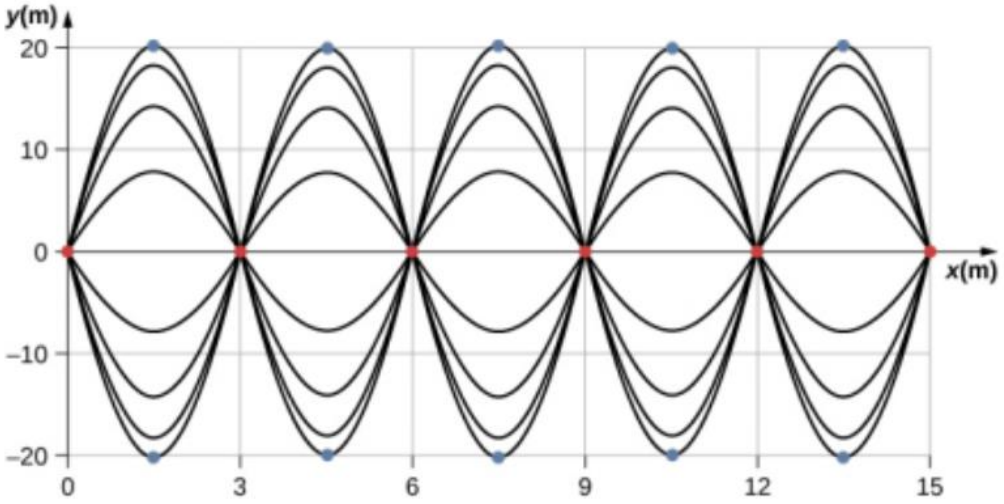

Figure 2.2. Diagram of a standing wave. Reprinted from [18].

As shown in the figure above, when two identical waves are moving in opposite directions, the resultant wave is a standing wave. It is important to note that nodes (represented by the red dots) appear at integer multiples of half wavelengths and is where the pressure does not change. Antinodes (represented by the blue dots) appear at odd multiples of quarter wavelengths and oscillate between the positive and negative values of the pressure wave's amplitude [18].

A standing wave can either be created using one transducer and reflecting the signal back or by using two transducers that play the same signal in opposite directions. Kozuka et al. [19] were successful in creating a powerful standing wave using two transducers. At a frequency of 39.9 kHz, their experiment created a standing sound pressure wave that can suspend polystyrene particles. The images depicted in Figure 2.3 help visualize the authors' work:

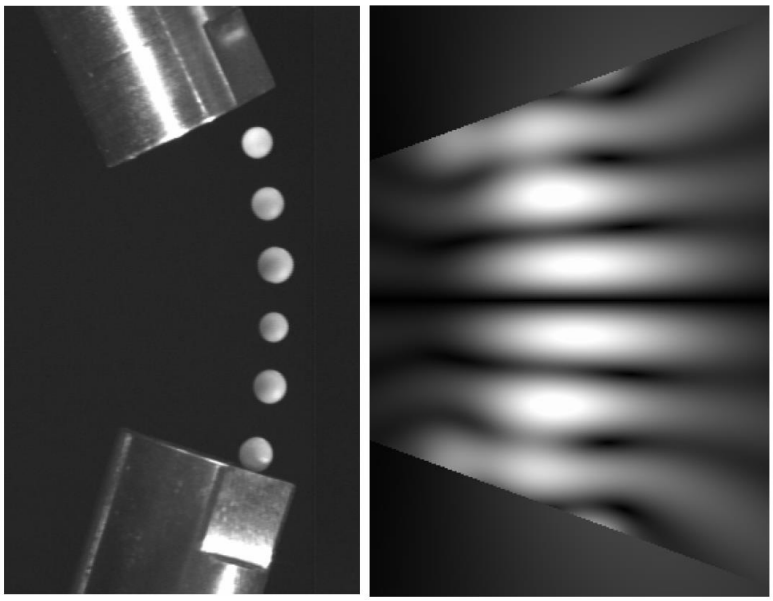

Figure 2.3. Polystyrene particles suspended in standing wave (Left). Calculated sound pressure distribution in the standing wave field (Right). Reprinted from [19].

These works inform our decision to use pairs of opposing transducers in our experiment to create a powerful standing acoustic wave with the goal of perturbing the boundary layer and thus affecting heat transfer.

Chapter 3

OVERVIEW OF EXPERIMENTAL APPERATUS

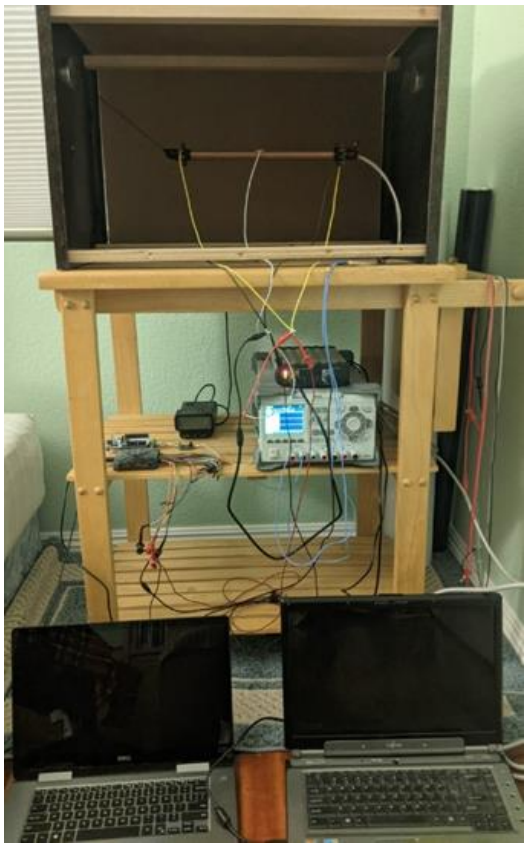

Figure 3.1. Image of experimental apparatus.

The primary purpose of the experimental apparatus (shown in Figure 3.1) is to test the effects of ultrasonic waves on natural convection heat transfer in air. To accomplish this task, the apparatus needs to perform three distinct functions. First, the apparatus must generate a steady state isothermal cylinder in an environment appropriate for natural convection to occur. Second, it must create a standing ultrasonic wave that actuates the air surrounding the cylinder. Finally, it must be able to accurately measure and record temperature changes on the surface of the cylinder. All these functions must be able to be conducted both simultaneously and independently.

Each function is addressed by an individual subsystem. The *Temperature Sensing Subsystem* is responsible for the measurement and recording of temperature data. The *Heating Subsystem* is responsible for generating the isothermal cylinder which undergoes natural convection heat transfer in air. The *Ultrasound Subsystem* is responsible for actuating the air surrounding the cylinder with an ultrasonic standing wave. The block diagram shown in Figure 3.2 illustrates the interactions between each subsystem. Note that the heating subsystem exposes the ultrasound subsystem to high temperatures which, if not addressed, could impact the functionality of certain electronics.

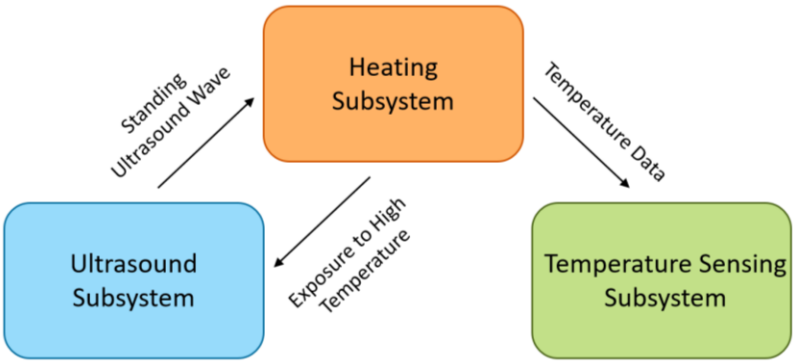

Figure 3.2. Block diagram of subsystem interaction.

The major components within each subsystem are detailed in Figure 3.3. The arrows in the diagram show the interactions between the components. The direction in which information or data flows between the components is indicated by the direction of the arrowheads. The solid arrow lines represent directly wired connections, whereas the dashed arrow lines represent wire-less information exchange.

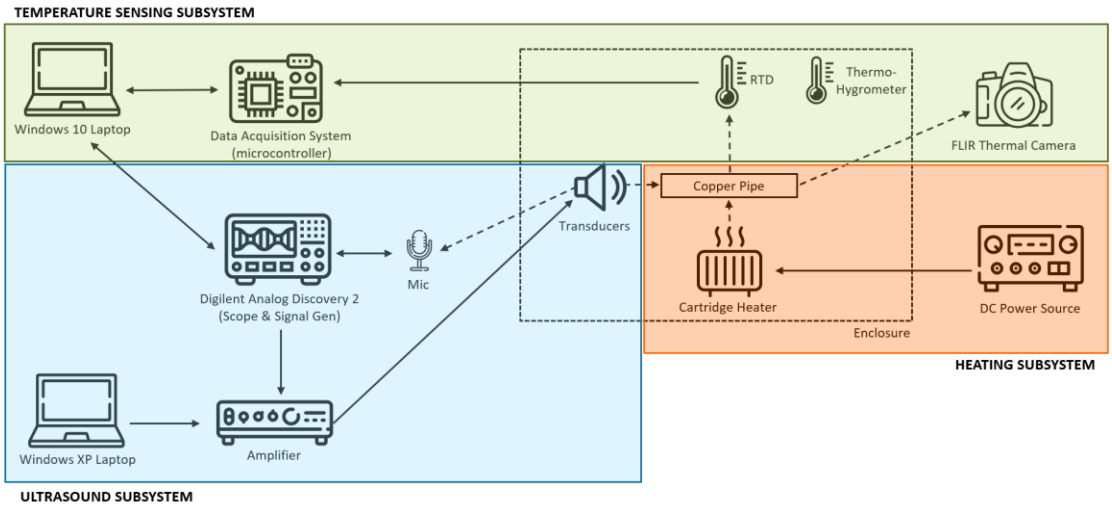

Figure 3.3. Diagram of experimental apparatus subsystems.

The temperature sensing subsystem, highlighted in the green box in Figure 3.3, has the capability of measuring and recording the cylinder surface temperature as well as the ambient air temperature. The cylinder surface temperature is measured with a RTD assembly and a thermal camera, while the ambient temperature is measured with a thermo-hygrometer. The heating subsystem is highlighted in the orange box. It approximates an isothermal cylinder with a cylindrical cartridge heater, incased in a copper pipe, and powered by a DC power supply. This subsystem also features an enclosure, represented by the dashed box, which ensures that the ambient air remains quiescent during the experiment. The blue box highlights the ultrasound subsystem. Here, a signal generator and amplifier assembly actuate ultrasound transducers to create a standing. The ultrasound subsystem also has a microphone connected to an oscilloscope allowing for the verification of the ultrasound wave. The temperature sensing, heating, and ultrasound subsystems are described in further detail in Chapters 4, 5, and 6, respectively.

Chapter 4

TEMPERATURE SENSING SUBSYSTEM

The temperature sensing subsystem was designed to collect temperature data during the experiment. As seen in Figure 4.1 below, there are three primary temperature-sensing devices in this subsystem: a digital thermo-hygrometer, a RTD assembly, and a thermal camera.

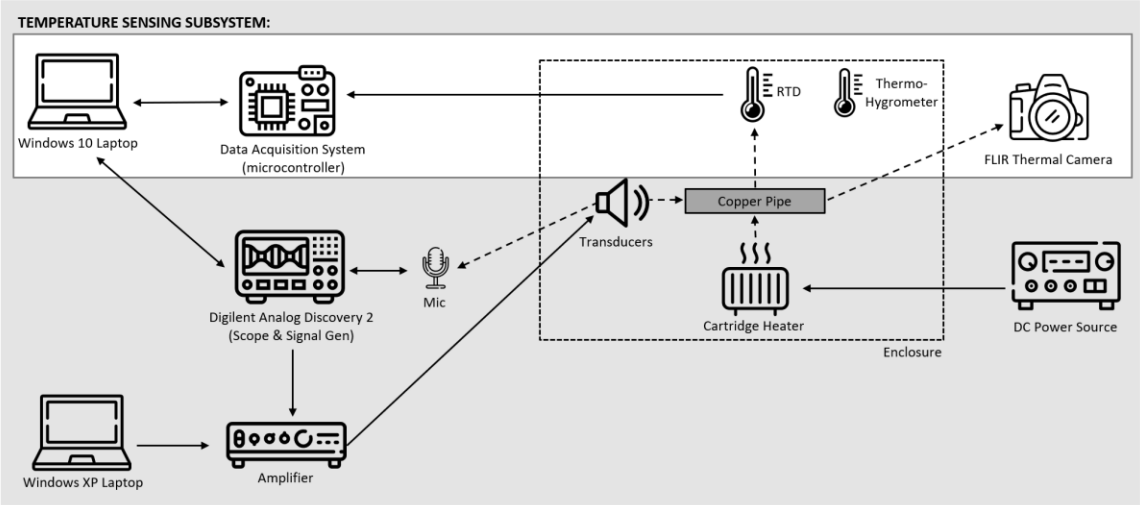

Figure 4.1. Diagram of experimental apparatus with temperature sensing subsystem highlighted.

The OMEGA Digital Thermo-Hygrometer is a self-contained device used to measure the ambient temperature and humidity within the enclosure. The Thermo-Hygrometer sensor is shielded from thermal radiation by a perforated metal enclosure. The RTD Data Acquisition System consists of a RTD and microcontroller assembly interfacing with a Windows 10 Laptop. The RTD system was used to measure and record the surface temperature of the copper pipe. It is discussed in more detail in Section 4.1 to follow. The

FLIR C5 Thermal Camera is a stand-alone device used to take thermal images of the copper pipe. Its use is discussed in more detail in in Section 4.2.

4.1 RTD Data Acquisition System

The purpose of the Resistive Temperature Detector Data Acquisition System (RTD DAQ System) is to measure and record the surface temperature of the copper pipe over time. The system consists of four primary components: the RTD, a RTD-to-digital converter chip, a microcontroller, and a Windows 10 computer running Tera Term software. A temperature change is first sensed by an OMEGA SA1-RTD Surface-Mount RTD Temperature sensor which experiences a corresponding change in resistance. This RTD resistance is then converted to a digital signal by the MAX31865 RTD-to-Digital Converter sampling at a rated 47.6 samples per second. The digital signal is then processed by the STM32 microcontroller and logged via a serial connection to the computer. The temperature data is then recorded over time using Tera Term's logging feature.

4.1.1 RTD DAQ System Construction

The RTD DAQ System is constructed as shown in Figure 4.2. The connections between the RTD-to-Digital Converter and the microcontroller are facilitated by custom breakout boards that were designed and assembled by Dr. John Ridgely from California Polytechnic State University. Dr. Ridgely also wrote the code for the microcontroller temperature processing.

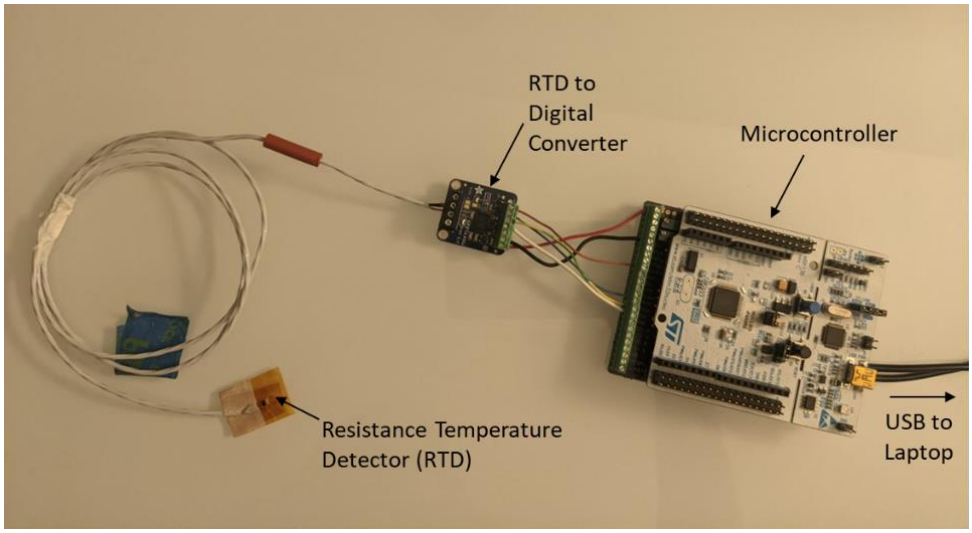

Figure 4.2. Image of assembled RTD DAQ System.

The RTD is connected to the ground, power, and data terminals on the RTD-to-Digital Converter via a terminal block. The RTD-to-Digital Converter is connected to the microcontroller's breakout board by six wires: power, ground, and a four-wire SPI serial connection. Finally, the microcontroller is connected to the Windows 10 computer by a Micro-USB to USB cable.

4.1.2 RTD Functionality and Accuracy Check

When assembling the RTD DAQ System, there were eleven available OMEGA SA1-RTDs. To assess the devices' functionality and accuracy, and to determine which would be best suited for our experiment, we conducted a two-point calibration check. Each RTD (numbered 1 – 11), was used to take the temperature of distilled water at freezing (~ 0℃) and boiling (~ 100℃). Figure 4.3 shows the test set-up for the Ice Bath and Boiling Bath temperature checks.

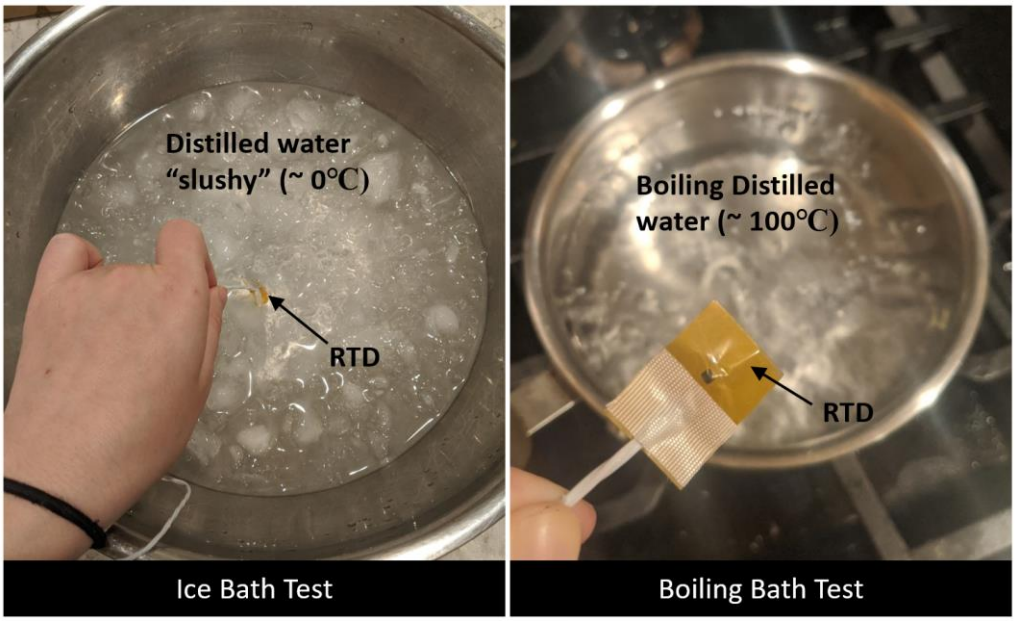

Figure 4.3. RTD reading check test set-ups at ~0°C (Left) and at ~100°C (Right).

The purpose of the Ice Bath Test is to check the accuracy of the RTD readings at near 0°C conditions. To do this we made an ice bath using distilled water (which should theoretically have a freezing point of 0°C). The ice bath was created by mixing crushed ice made from distilled water and refrigerated distilled water. The mixture was combined in a stainless-steel bowl that had been cleaned using distilled water. One at a time, each RTD was fully submerged in the ice bath such that it did not touch the sides of the bowl. Then a temperature reading was taken. Between each new RTD, the ice bath was stirred with a silver spoon and more ice was added as needed.

The purpose of the Boiling Bath Test is to check the accuracy of the RTD readings at near 100°C conditions. To do this we made a boiling bath using distilled water (which should theoretically have a boiling point of 100°C; the experiment was conducted in San Luis Obispo at an elevation of approximately 320 feet). The boiling bath was created by

bringing distilled water to a boil on a gas stove burner in a clean stainless-steel pot. One at a time, each RTD was fully submerged in the boiling bath such that it did not touch the sides of the pot. Then a temperature reading was taken.

Both the Ice Bath and the Boiling Bath Tests were performed over a two-hour period. The temperature readings from each RTD for both tests can be seen in Table 4.1.

Table 4.1. Temperature readings from each RTD for the Ice Bath and Boiling Bath Tests.

RTD Number	Temperature at Freezing ℃ (±0.15 ℃)	Temperature at Boiling ℃ (±0.15 ℃)
1	0.0	96.6
2	0.4	96.6
3	-0.2	97.2
4	N/A	N/A
5	N/A	N/A
6	0.2	99.1
7	0.2	97.1
8	0.4	97.0
9	0.3	96.6
10	-0.1	97.2
11	0.2	97.0

Based on the readings presented in Table 4.1, RTD Number 6 was selected for our experiment because it produced the most accurate reading out of all the RTDs for the Boiling Bath Test. It was more important to select a RTD based on its performance in the Boiling Bath Test than the Ice Bath Test, because our experiment will be operating at temperatures close to 100 ℃.

4.2 Thermal Imaging

Another method of temperature sensing employed in this subsystem was thermal imaging. The benefit of collecting thermal images during the experiment is that it does not require contact with the pipe in order to take a temperature reading. That way, the measurement does not impact the boundary layer formed around the pipe. Additionally, the images have the potential to provide a highly visual representation of the temperature distribution along and around the pipe. The disadvantage of thermal imaging is that the accuracy of the measurement is greatly affected by many factors including: the resolution of the thermal camera, the emissivity of the subject, and the distance and angle at which the image was taken. Due to these complications, it was expected that thermal imaging would produce only relative temperature data at best, and qualitative data at worst.

To highlight the challenges in obtaining thermal imaging data and images, we originally attempted to use the FLIR BOSON thermal camera, a model still in development but provided to us by the FLIR Corporation. However, we discovered after much testing that in its current product development stage, the BOSON was not yet configured to provide local temperature measurements. So, we procured a FLIR C5 Compact Thermal Camera, a model in commercial use for several years. The FLIR C5 is a self-contained device that can automatically adjust the temperature scale of an image and can store thermal images onboard. These images can later be copied to a computer using a USB connection and FLIR proprietary software. The thermal images captured by the camera in the course of the experiments were used for qualitative analysis in conjunction with temperature data acquired using the RTD DAQ System. Figure 4.4 shows the FLIR C5 camera and a sample thermal image of a lit candle taken with it. In the thermal image the blue and red crosshairs

show the locations of the lowest and highest temperatures in the image, respectively. The white crosshairs show the center of the camera's view and can be used to take a temperature measurement at a point of interest.

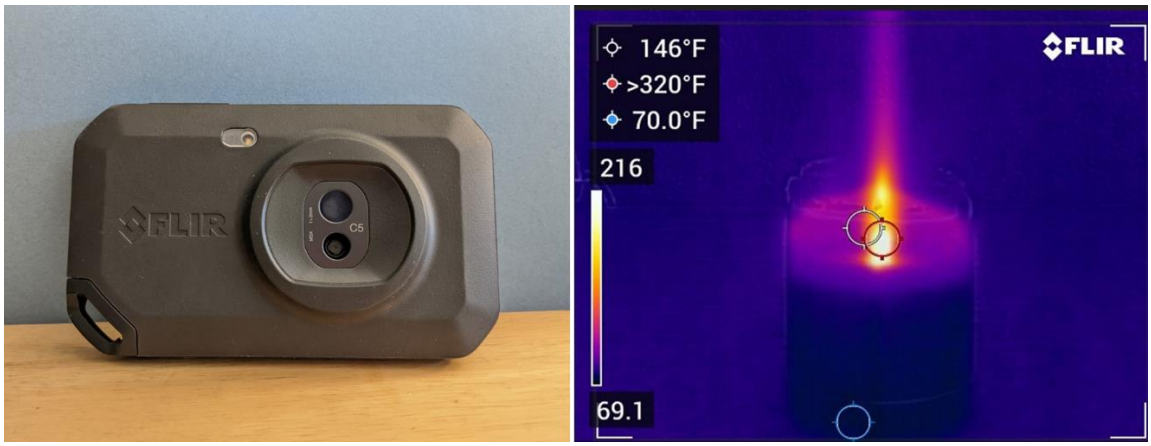

Figure 4.4. FLIR C5 thermal camera (Left) and sample thermal image of lit candle taken with FLIR C5 (Right).

Chapter 5

HEATING SUBSYSTEM

The purpose of the heating system is to provide a known, constant, and uniform heat flux along the pipe and to create an experimental environment that allows for natural convection from a cylinder geometry. As seen in Figures 5.1 and 5.2 below, there are two main components to the heating subsystem: the enclosure and the heated pipe assembly.

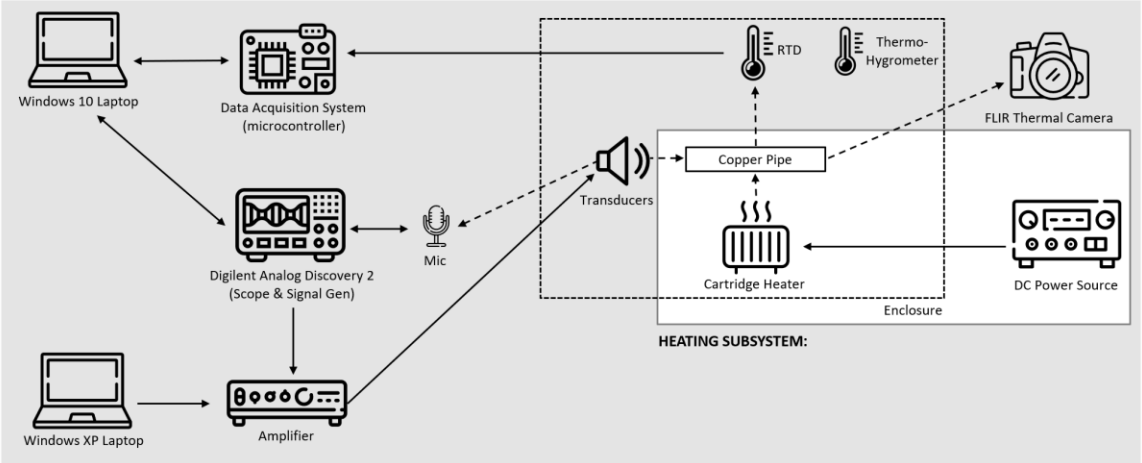

Figure 5.1. Diagram of experimental apparatus with heating subsystem highlighted.

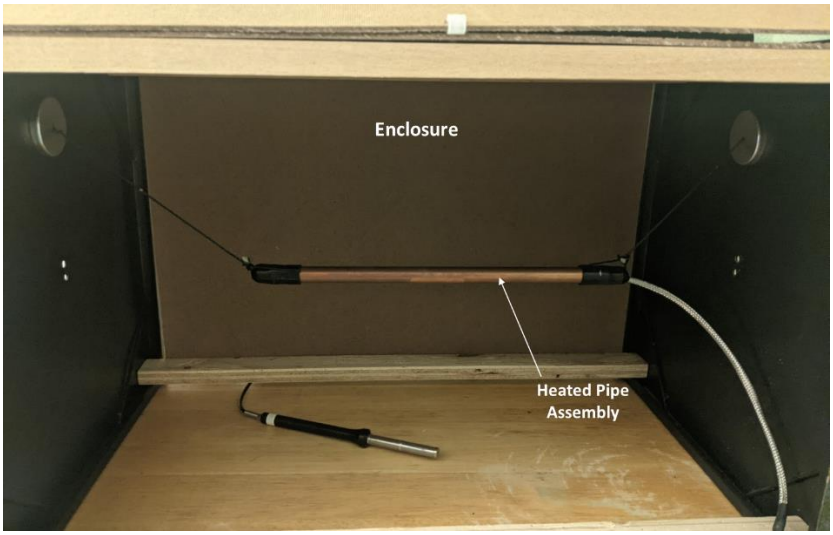

Figure 5.2. Image of heating subsystem.

The enclosure is a box-like structure which protects the experiment from ambient breezes which may alter the natural convection heat transfer process. It allows for the suspension of the copper pipe in the center of the enclosure and additionally encompasses the RTD, the Thermo-Hygrometer probe, and ultrasound transducers. The enclosure is discussed in further detail in Section 5.1.1. The heated pipe assembly consists of a cylindrical cartridge heater surrounded by a copper pipe and powered by a DC power supply. This assembly allows for the experiments to be run with a constant heat flux and is discussed in more detail in Section 5.1.2.

5.1 Heating Subsystem Design and Construction

This section discusses the construction of the two heating subsystem components: the enclosure and the heated pipe.

5.1.1 Enclosure Design and Construction

The primary purpose of the enclosure is to ensure that the quiescent ambient air surrounding the experiment is not disturbed by external air currents. This helps to provide a suitable environment for natural convection. In the original conception of this experiment, we intended to use a pre-existing aluminum enclosure found in Cal Poly's Thermal Sciences Laboratory. However, due to the campus-wide lab closures in response to the COVID-19 pandemic, an alternative enclosure had to be constructed for use in a residential home.

The enclosure was built primarily of materials sourced from a local hardware store including: a 0.5 inches by 1.5 inches wooden beam with a length of 8.5 feet, two 2 foot by

4 foot hardboard panels, three plastic cable clamps, nine #5 Philips head wood screws, and eight #8 slotted hex head screws with corresponding washers. Additionally, two 16 inches by 16 inches magnetic metal panels were obtained. To construct the enclosure, the wooden beam was first cut into four parts each measuring approximately 25 inches in length. Then, using a hand-held drill, pilot holes were drilled centrally into both ends of each wooden beam part. Four pilot holes were also drilled into each of the metal plates, located near every corner 1 inch from each adjoining side. The metal plates and wooden beam parts were then assembled using the #8 slotted hex head screws and washers, to create the frame shown in Figure 5.3.

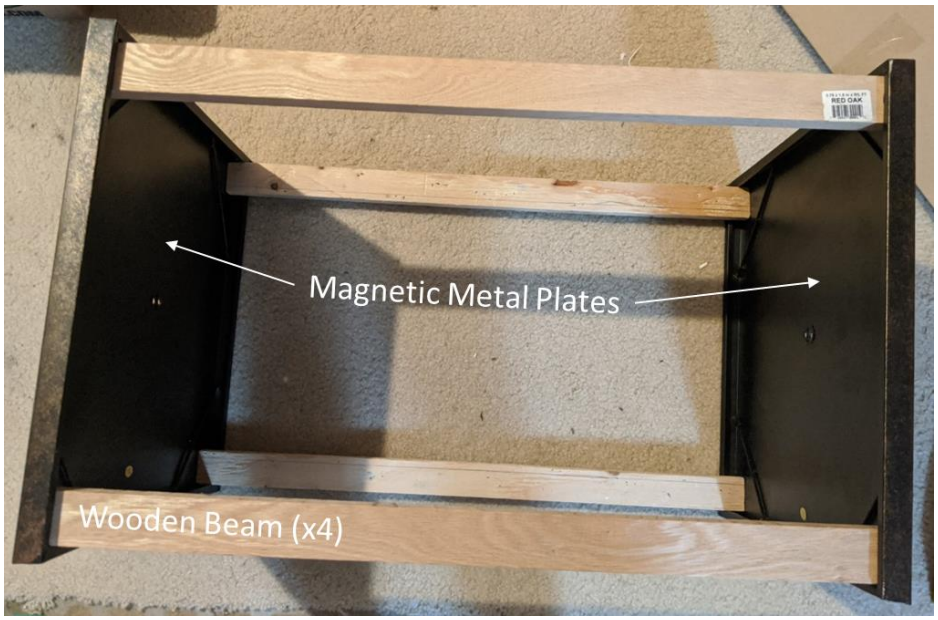

Figure 5.3. Enclosure frame.

Next, the hardboard panels were cut to create three smaller panels, each with dimensions of 24 inches by 15 inches. Then, one of the panels was placed so that it rested flat against the wooden beams on one side of the enclosure frame. After ensuring that the length of the panel was parallel with the length of the beams, the hardboard was screwed

to the wooden beams at each corner using four of the wood screws. A similar process was repeated for the second side of the enclosure frame, but with the addition of three plastic cable clamps and a fifth wood screw. Along the length of the second side facing the sides of the enclosure not yet covered with hardboard, a plastic cable clamp was attached to each corner of the hardboard with the same screw that attaches the hardboard to the wooden beam. Additionally, a third cable clamp was attached to the hardboard halfway along the same length using a wood screw. The third hardboard panel acts as a door to the enclosure. Using a Dremel, three oblong holes were cut out of the hardboard approximately 1cm from the top and spaced such that they line up with the cable clamps. The panel was then hung from the top side of the enclosure from the cable clamps. The cable clamps act as a kind of door hinge, allowing the panel to swing up and provide access to the enclosure. Figure 5.4 shows the fully constructed enclosure.

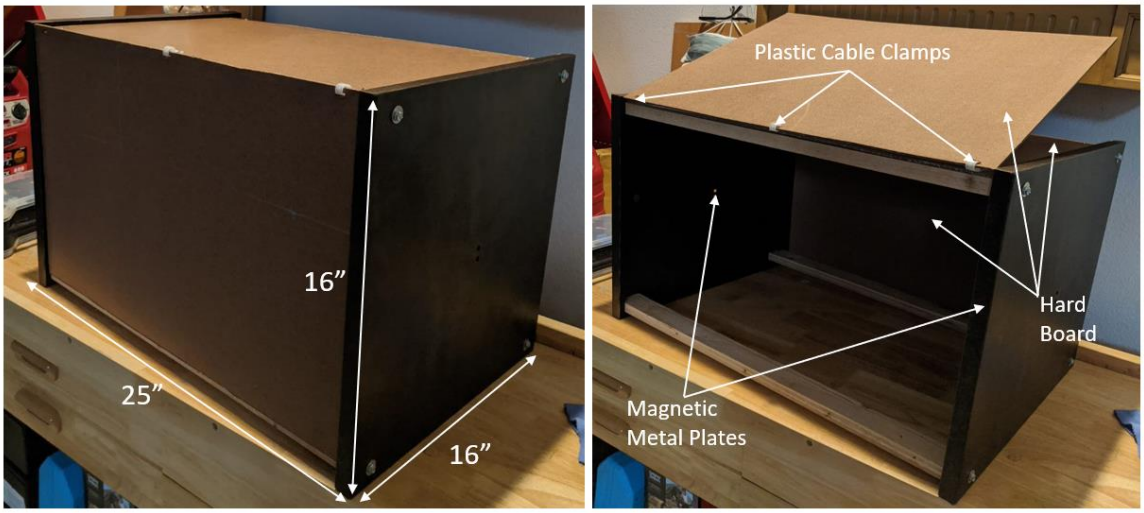

Figure 5.4. Enclosure closed (Left). Enclosure open (Right).

5.1.2 Heated Pipe Design and Construction

The heated pipe assembly was designed to, under steady state conditions, approximate an isothermal cylinder with a constant heat flux. It is comprised of the following components: a 1/2 inch-diameter Type-M copper pipe, cartridge heater, a RIGOL DP832 DC Power Supply, two 1/2 inch silicone plugs, two 5/8 inch silicone caps, Kevlar string, and two large magnets. A diagram of the heated pipe assembly is shown in Figure 5.5, and image of the assembly is shown in Figure 5.6.

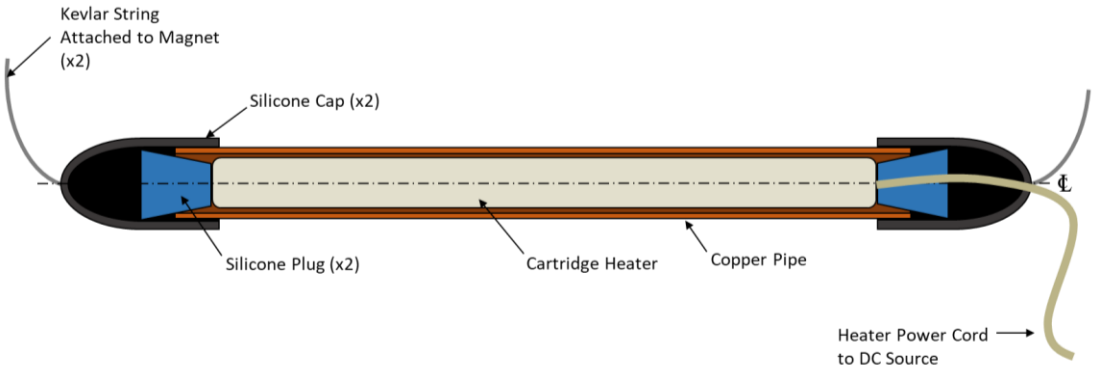

Figure 5.5. Cross-sectional diagram of the heated pipe assembly.

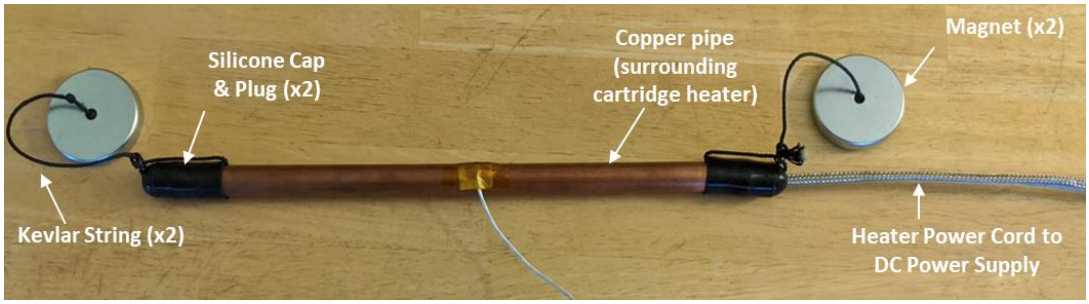

Figure 5.6. Image of heated pipe assembly.

A copper pipe was selected as part of this design for three main reasons. First, the external geometry is the same as that of a cylinder and has been used to approximate a cylinder in other studies examining the effects of ultrasound on heat transfer [9]. Second,

the hollow nature of the pipe allows for a heater to be inserted to provide even heating and reduce any thermal gradients along the length of the pipe. Third, the material properties of copper are well studied and available for our analysis. A Type-M copper pipe was specifically selected because it has the thinnest wall thickness of all commercially available copper pipes at a thickness of .032 inches. The thin wall will reduce the axial and angular conduction, thus reducing end effects and resembling an infinitely long pipe. This allows us to better replicate the conditions inherent in the standard heat transfer correlations.

A two-foot-long Type-M copper pipe with a ½ inch nominal diameter was sourced from a local hardware store. The pipe was cut into two parts each with a length of 12 inches. One part was sprayed with three coats of Rust-Oleum Specialty High Heat Matte Black Bar-B-Que Spray Paint, while the other was left in its original condition with a shiny metal finish. These pipes, with their two different surface finishes, serve two different purposes in the experiment. The matte black pipe, which has a high emissivity, is for use with the thermal camera. Thermal cameras require relatively high emissivity surfaces to properly capture a subject. The blackened surface will likely increase thermal radiation emitted from the pipe, so the pipe with the shiny metallic finish is useful because its shiny surface allows us to approximate thermal radiation from the pipe to be negligible. The efficacy of this assumption will be tested when verifying the heat transfer from the experimental apparatus against theory, which presented in Section 2.2.

The cartridge heater was sourced from McMaster-Carr (part number 4877K383). This cartridge heater was selected because it is specified for a ½ -inch hole which matches the chosen pipe diameter. To extend the distance the cartridge heater can be from the power supply, an additional two feet of 18 AGW stranded core wire was soldered to the ground

and power cords. The cartridge heater is placed concentrically inside the copper pipe, where it provides the system with a constant heat flux when powered by the DC power supply.

Both ends of the pipe are then closed off with a silicone plug. The plug on side of the pipe from which the power cord extends has a hole in it that allows the power cord to pass through with a tight interference fit. The purpose of the silicone plugs is twofold. First, they reduce the amount of heat which can escape from inside the pipe, allowing for a better approximation of an isothermal cylinder. Second, they further center and secure the cartridge heater in the pipe.

Silicone caps are placed on top of the silicone plugs, slightly overlapping the ends of the pipe. Although the caps also help reduce the amount of heat which escapes from inside the pipe, their primary purpose is to provide location where the ultrasound transducers can be mounted. Because silicone is an excellent thermal insulator, it prevents the transducers from being greatly affected by the high pipe temperature.

The silicone caps also play an important role in the mechanism used to suspend the heated pipe within the enclosure. The ends of both caps were punctured to allow for a piece of Kevlar string to be tied around each. This allows one end of the Kevlar string to be anchored to the pipe by the silicone cap. The other end of each Kevlar string is tied to a large magnet. Kevlar string was chosen specifically for its strength and low thermal conductivity. These magnets can be attached to the magnetic plates of the enclosure, thus suspending the heated pipe assembly as shown in Figure 5.7.

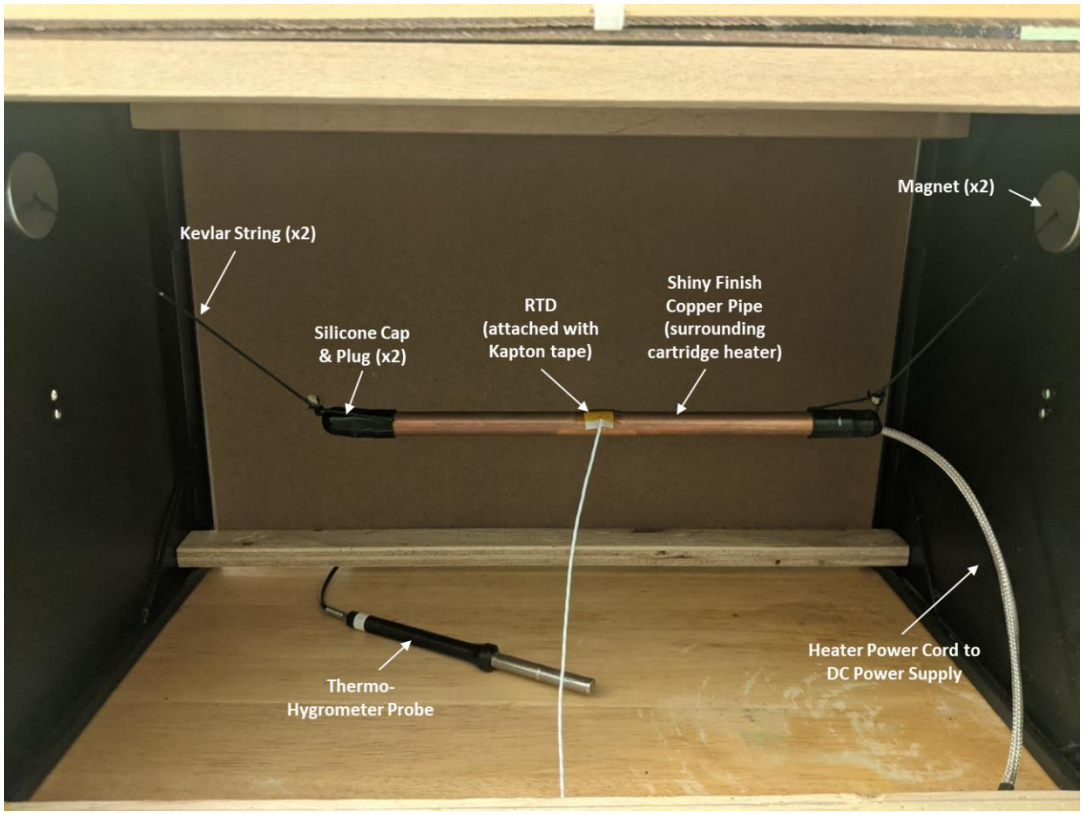

Figure 5.7. Heating Subsystem assembled with portions of the Temperature Sensing Subsystem.

5.2 Heating Subsystem Verification

To verify that the heating subsystem was functioning as expected, two tests were performed. The first was a *Natural Convection Check* to see if the system reached the expected steady state temperature. The second was a *Forced Convection Check* used to see if the system would respond appropriately to a change in the flow regime. The Natural and Forced Convection checks are discussed in more detail in Sections 5.2.1 and 5.2.2, respectively.

5.2.1 Natural Convection Check

The goal of the Natural Convection Check is to verify the system's experimental steady state surface temperature against the expected theoretical temperature. The shiny finish metal pipe was used so radiation heat transfer could be considered negligible and the data could be compared to the correlations presented in [13,15]. Temperature data was taken continuously from the pipe surface with the RTD assembly. Ambient temperature was recorded from the thermo-hygrometer probe to be 26°C, and the power into the system was 14.82 W read from the power supply. The test was conducted with the enclosure door closed to reduce the impact of the external environment on the ambient air. The experimental set-up inside the enclosure can be seen in Figure 5.8.

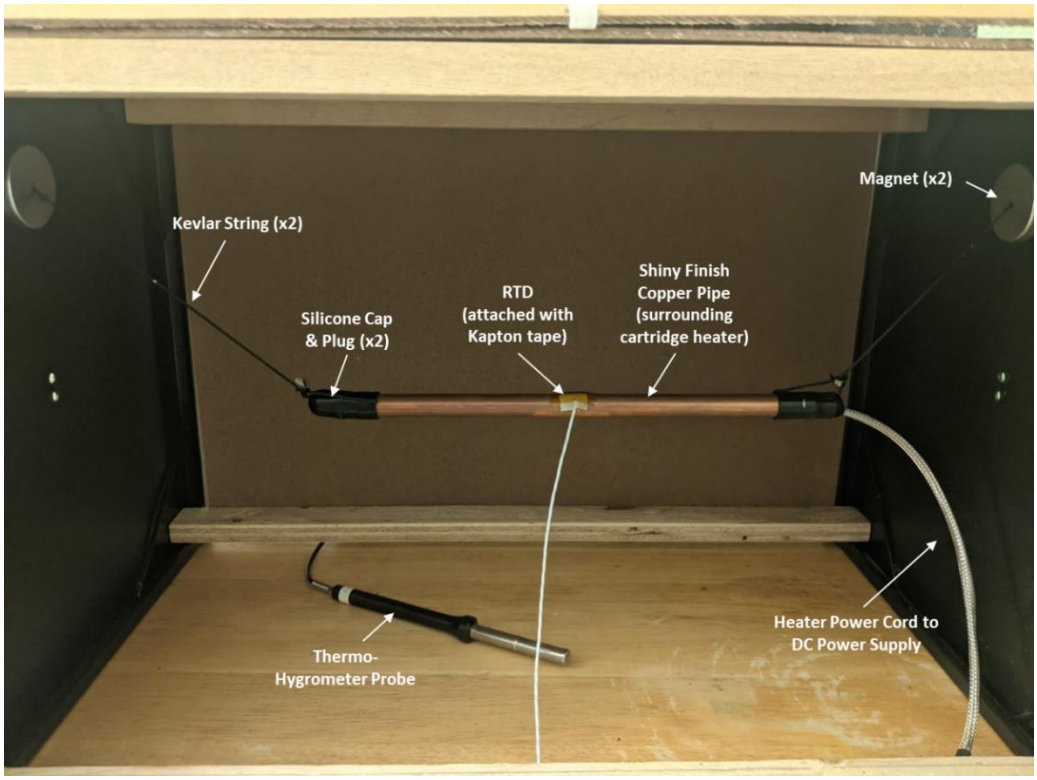

Figure 5.8. Test set-up for Natural Convection Check.

Using an iterative method in Excel, Equations 2.1 through 2.7 presented in Section 2.2 were solved using the given experimental conditions to determine the expected theoretical steady state surface temperature. The Churchill and Chu correlation [13] predicts a steady-state surface temperature of 113℃, and the Morgan correlation [15] predicts a surface temperature of 106.3℃. The calculation for the final iterations for both correlations is presented in Appendix A. The experimental steady state surface temperature was recorded to be 104.92℃. Plots of the experimental heating curve and the theoretical steady state temperature from each correlation are shown in Figure 5.9.

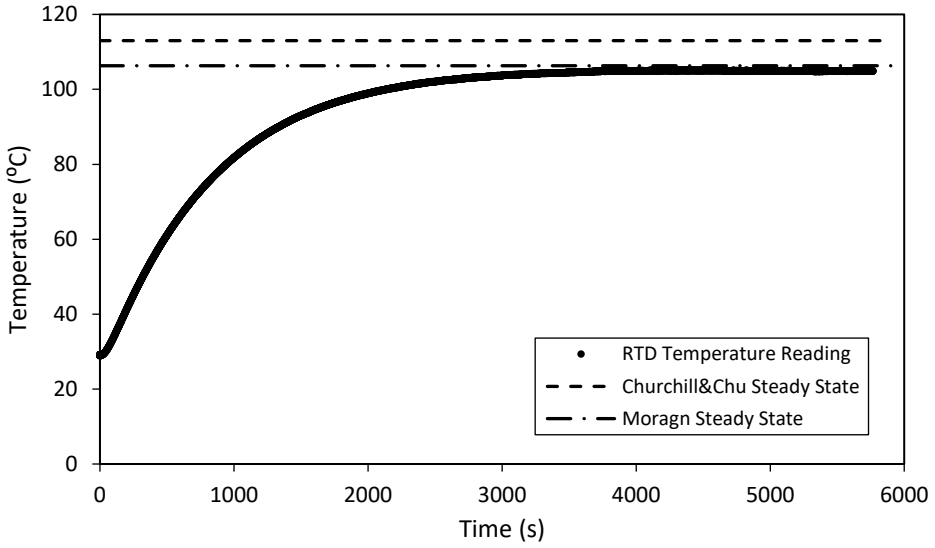

Figure 5.9. Plot of measured pipe surface temperature and the theoretical steady state surface temperature.

There is approximately an 8℃ and 1.38℃ difference between the measured steady state surface temperature and the expected theoretical values from the Churchill and Chu and Morgan Correlations, respectively. The measured surface temperature and the theoretical surface temperature determined by the Morgan correlation agree. Morgan reports that the correlation has an uncertainty of ± 5% for the Nusselt number [15], which

corresponds to a valid temperature range of 103℃ to 111℃. The measured steady state surface temperature of 104.92℃ falls in that range. No correlation accuracy was reported for the Churchill & Chu correlation, so we conservatively estimate an uncertainty of ± 10% for the Nusselt number. For this uncertainty the Churchill and Chu correlation has a valid temperature range of 105℃ to 123℃. The measured surface temperature is very close to the estimated lower bound of the correlation. The apparent agreement between measured and theoretical steady state temperatures gives us confidence that the experimental apparatus is functioning as expected.

Figures 5.10 and 5.11 show the plots of $T_s - T_\infty$ and the heat transfer coefficient, respectively, both as a function of heat flux (q").

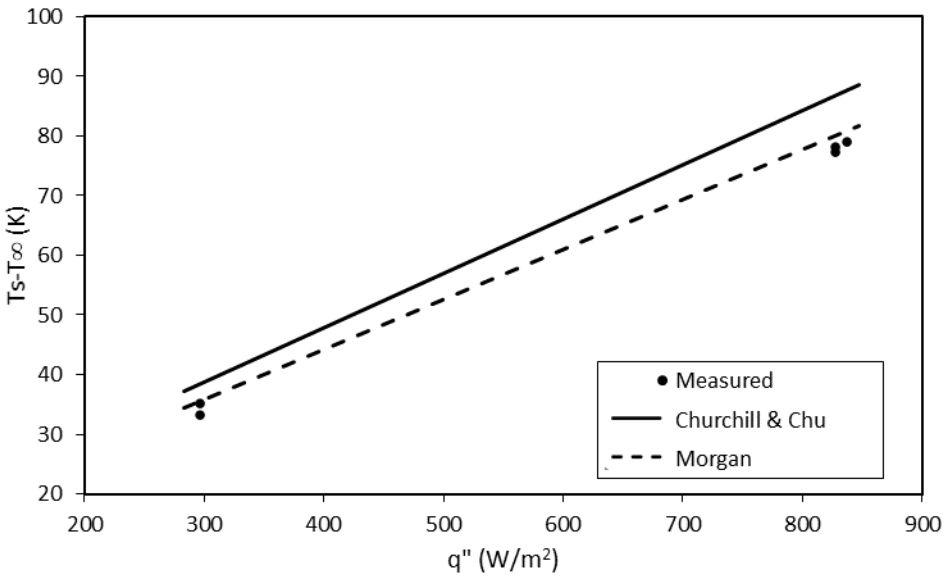

Figure 5.10. Difference in steady state surface temperature (T_s) and ambient temperature (T_∞) as a function of heat flux (q").

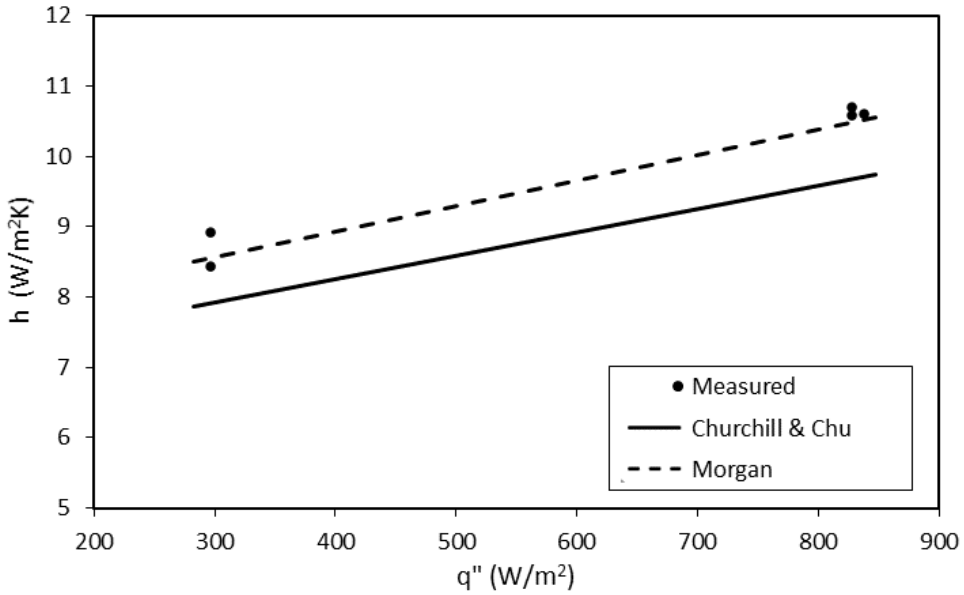

Figure 5.11. Heat transfer coefficient (h) as a function of heat flux (q").

The plots in Figures 5.10 and 5.11 compare the measured temperature and coefficient of heat transfer values against those predicted by the Churchill and Chu and Morgan correlations. In both figures the theoretical and measured values agree, with the largest difference falling within the ±5% uncertainty of the Morgan correlation. It is important to note that there is an apparent trend, for the measured values indicate a higher rate of cooling than the correlations estimate. The measured $T_s - T_\infty$ values shown in Figure 5.10 fall below the predicted temperature difference from both correlations. Additionally, the measured heat transfer coefficients shown in Figure 5.11 are generally higher than those predicted by the correlations. This trend may be due to additional heat loss from the ends of the pipe. Ultimately, however, this test supports that the experimental apparatus is functioning as expected under natural convection heat transfer.

5.2.2 Forced Convection Check

We anticipated that introducing sound waves to the air surrounding the cylinder could produce a weak cooling effect, so the goal of the Forced Convection Check is to verify the system's response to a significant change in airflow from quiescent air to a forced air regime. The shiny finish metal pipe was used, and temperature data was taken continuously from the pipe surface with the RTD assembly. Ambient temperature was recorded from the thermo-hygrometer probe to be 22℃. The power into the system was 14.70 W read from the power supply. The test was conducted with the enclosure door closed to reduce the impact of the external environment on the ambient air. The experimental set-up is similar to that of the Natural Convection Check, but additionally features a Noctua NF-A9x14 PWM fan placed approximately 5 inches below the pipe underneath the RTD. The set-up is shown in in Figure 5.12.

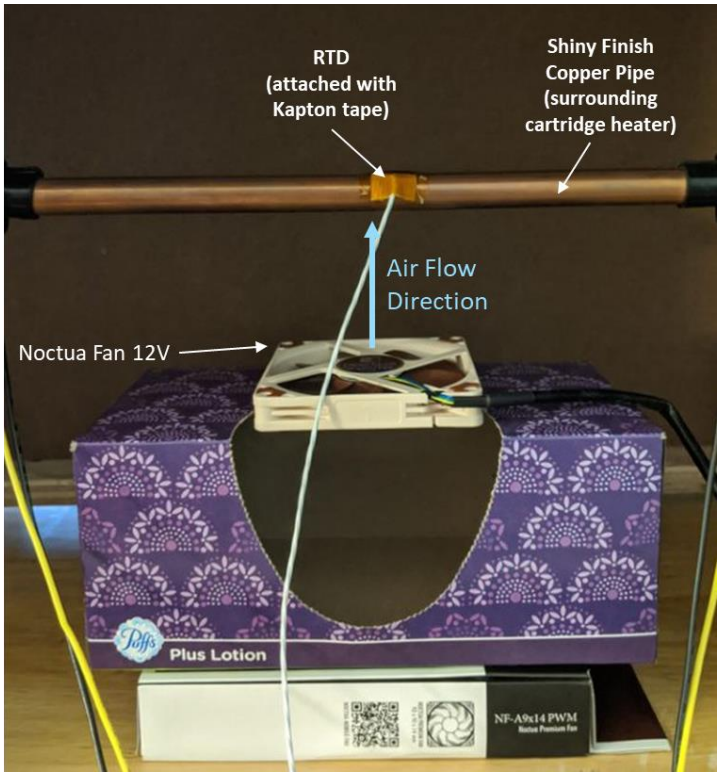

Figure 5.12. Test set-up for Forced Convection Check.

During the test, the system was first allowed to reach its steady state condition before the fan was powered with 12V DC from the power supply. The system approaches a steady state surface temperature of approximately 100°C. It is interesting to note that this measured value is also within the expected temperature range predicted by the Morgan correlation [15] for the given conditions. After steady state was reached, the fan was turned on. The response of the system is graphed in Figure 5.13, where the vertical dashed line represents the time at which the fan was powered on.

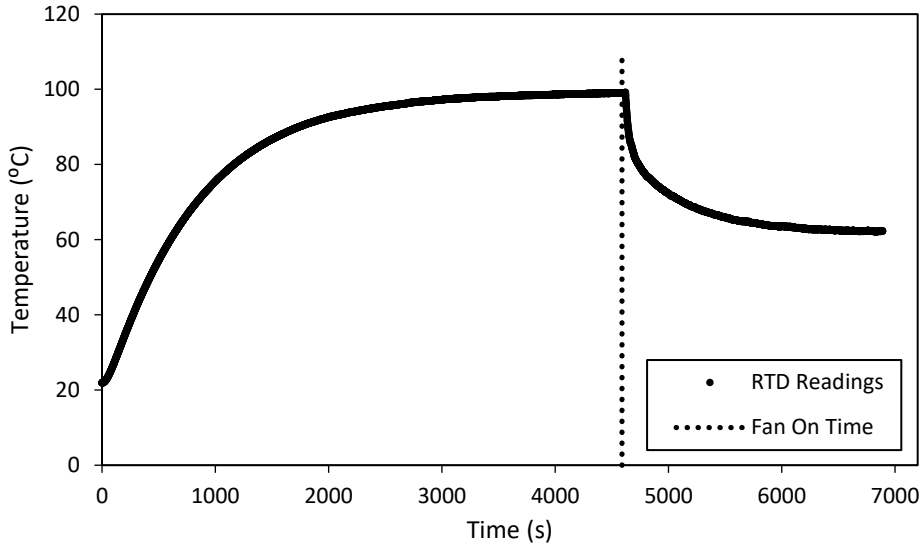

Figure 5.13. System surface temperature response to forced convection.

The response shown in Figure 5.13 is what we would expect from a heated cylinder experiencing a near-instantaneous change from natural convection in quiescent air to forced convection in crossflow. The surface temperature drops off rapidly form the natural convection steady state once the fan is powered on. Then, after some time, the system reaches a new steady state surface temperature corresponding to the crossflow conditions. These results give us confidence in two things. The first is that the system is responding

appropriately to changes in the surrounding environment, and the second is that the RTD assembly is able to detect changes in the pipe surface temperature.

Chapter 6

ULTRASOUND SUBSYSTEM

The ultrasound subsystem was designed to actuate the air surrounding the heated pipe with a standing ultrasound wave. As seen in Figures 6.1 below, there are two main components to the ultrasound subsystem: the microphone (sensing) assembly and the ultrasound transducer assembly.

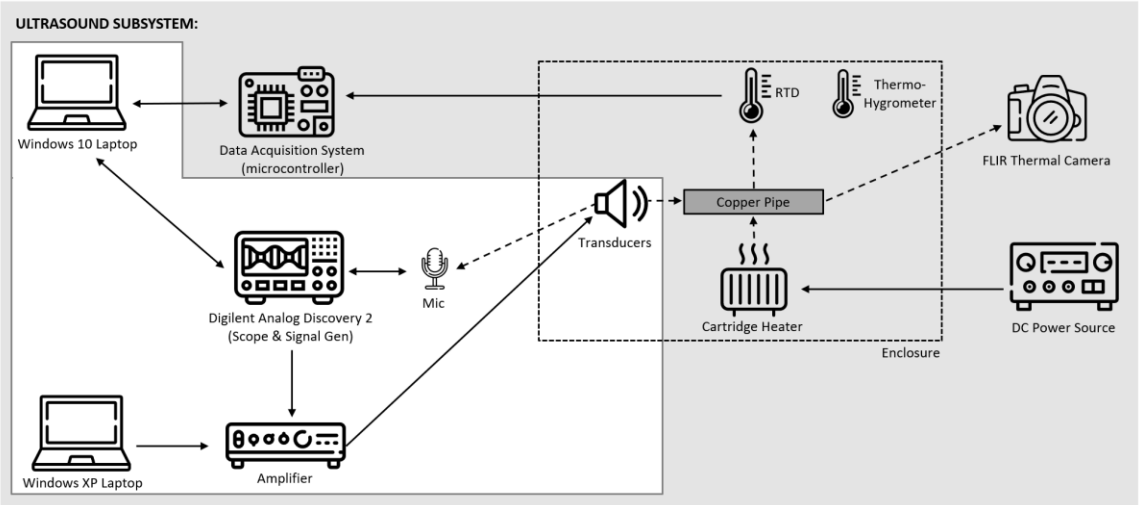

Figure 6.1. Diagram of experimental apparatus with ultrasound subsystem highlighted.

The microphone assembly is composed of a MEMS microphone and a Digilent Analog Discovery 2 unit acting as an oscilloscope by interfacing with a Windows 10 Laptop. The microphone assembly was used to assess and capture the properties of the ultrasound waves. It is discussed in further detail in Section 6.1 to follow. The ultrasound transducer assembly consists of sixteen 40 kHz ultrasound transducers, an amplifier (whose drivers required interfacing with a Windows XP computer), and a Digilent Analog Discovery 2 acting as a signal generator by interfacing with a Windows 10 Laptop. The assembly's design and construction is discussed in Section 6.2

6.1 Microphone Assembly

The purpose of the microphone assembly is to measure and capture the acoustic waves produced by the system with minimal disturbance to the signal. The assembly consists of three primary components: the CUI Devices CMM-2718AB-38108-TR MEMS Microphone, the Diligent Analog Discovery 2 hardware acting as an oscilloscope and a power source, and the Windows 10 computer running WaveForms software.

The MEMS (Micro-Electro-Mechanical Systems) microphone measures 2.75 by 1.85 by 0.95 mm and was selected because of its small size and broad bandwidth. Its small size is desirable because it reduces the impact it has on the acoustic signal, which at 40 kHz has a wavelength of 8.6 mm. The wide bandwidth is important because it allows us to read the 40 kHz signal produced by the transducers. Other microphones with smaller bandwidths may not have the ability to capture a frequency in that range. To sense an acoustic wave, the microphone measures the pressure difference the wave creates in the air and generates a corresponding electrical signal.

The signal is sensed by the Analog Discovery 2 unit which, in conjunction with the Windows 10 computer and WaveForms software, acts as an oscilloscope. When the design of this subsystem was initially conceived, we intended to use a bench-top oscilloscope to capture measurements of the ultrasound waves. However, due to the campus-wide lab closures in response to the COVID-19 pandemic, this alternative oscilloscope was assembled for use in a residential home. Section 6.1.1 details how the microphone assembly was constructed.

6.1.1 Microphone Assembly Construction

The microphone assembly was constructed according to the circuit diagram shown in Figure 6.2. The microphone is supplied with 2 V_{DC} across the positive and ground terminals. An oscilloscope is connected between the output and ground terminals so that we can observe the microphone readings.

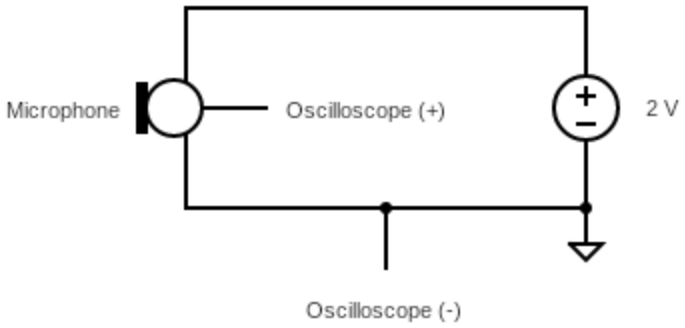

Figure 6.2. Circuit diagram of microphone assembly.

To properly wire the assembly, leads were soldered to the ground, power, and output terminals on the microphone. The process, as shown in Figure 6.3, was performed by hand and used 30 AWG multi-stranded copper wire. Due to the size of the microphone special care had to be taken while soldering to anchor the microphone in place and not to cause thermal damage to the electronics. The microphone and wires were held in place by Kapton tape, and soldering was completed as quickly as possible quickly to prevent damage.

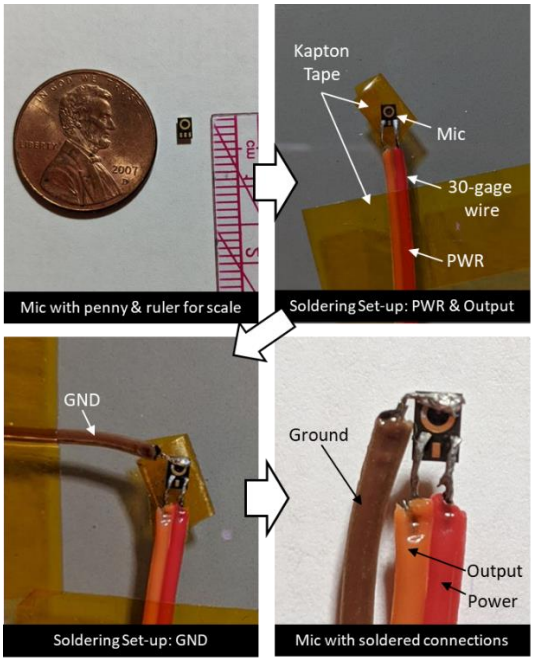

Figure 6.3. Microphone connection soldering process.

The final assembly was connected to the Analog Discovery 2 on a breadboard using jumper wires and is shown in Figure 6.4. The microphone is powered at 2V across the power and ground terminals and the sensed signal is read using the oscilloscope setting across the output and ground terminals.

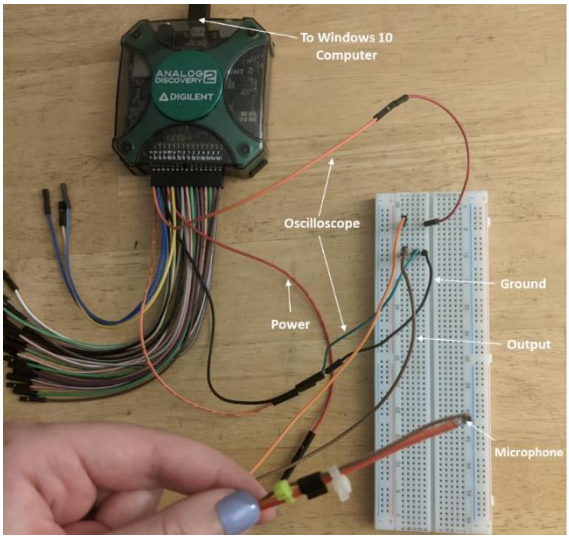

Figure 6.4. Microphone assembly constructed on a breadboard.

6.1.2 Microphone Check

To check the functionality of the microphone, a test was performed to see if it could properly sense a known signal. A 40 kHz signal was emitted for the test by a Manorshi Electronics MSO-P1040H07T transducer driven by the Analog Discovery 2 system. The circuit diagrams for the transducer and microphone are shown in Figure 6.5.

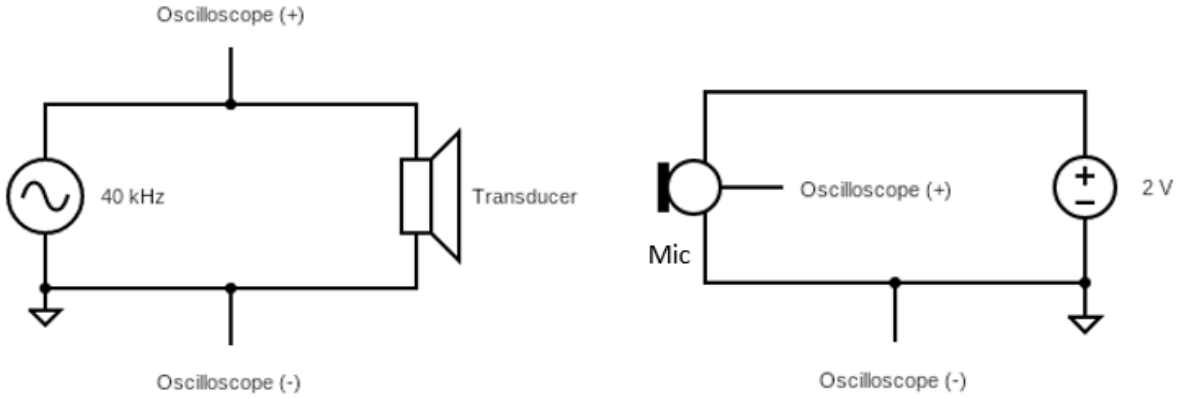

Figure 6.5. Circuit diagrams for the single transducer assembly (Left) and the microphone assembly (Right).

As shown in Figure 6.6, both the microphone and transducer circuits were assembled on a breadboard. The Analog Discovery 2 hardware generated a 1.6 V_{PP}, 40 kHz signal emitted by the transducer. The microphone was held above the transducer to sense the emitted sound wave.

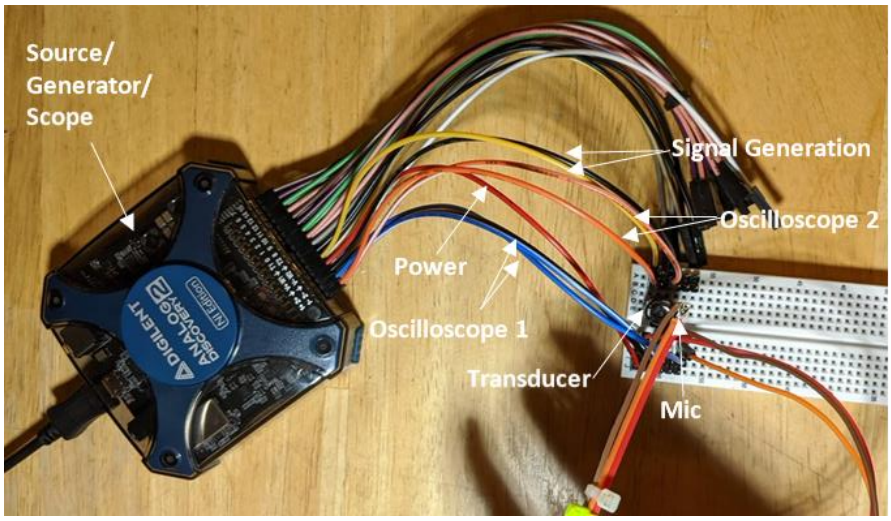

Figure 6.6. Microphone Check set-up.

The signal "heard" by the microphone was captured by the Analog Discovery's oscilloscope function. A scope capture showing the generated and sensed signals is shown in Figure 6.7. The signal sensed by the microphone was 39.99 kHz. This matches the generated 40kHz signal well (given the accuracy of the microphone and the hand-held nature of the set-up) and indicates that the microphone is in working order.

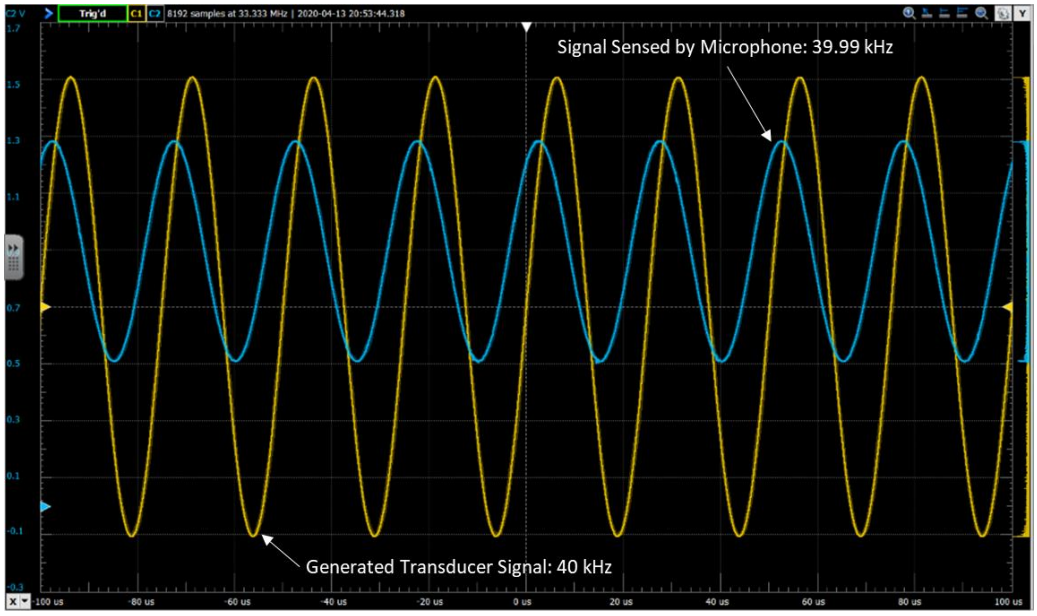

Figure 6.7. Oscilloscope capture of generated transducer signal and signal sensed by microphone.

6.2 Ultrasound Transducer Assembly

The purpose of the ultrasound transducer assembly is to create a strong, standing, 40kHz sound wave in the air surrounding the heated pipe. The assembly consists of five primary components: sixteen Manorshi Electronics MSO-P1040H07T transducers, the RIGOL PA1011 Power Amplifier interfacing with a Windows XP computer, the Diligent Analog Discovery 2 acting as an oscilloscope and a signal generator, and the Windows 10 computer running WaveForms software.

The 40 kHz transducers were selected for two main reasons. First, other investigators of the effects of ultrasound on heat transfer processes found success using a 40 kHz signal [8, 9]. Second, 40 kHz transducers are readily available on the consumer market, making them easy to source. To actuate the air along the pipe, the transducers were formed into two rings, each containing eight transducers. These transducer rings were powered by a signal generated by the Analog Discovery 2 and Windows 10 computer assembly. When the design of this subsystem was initially conceived, we intended to use a bench-top signal generator. However, due to the campus-wide lab closures in response to the COVID-19 pandemic, an Analog Discovery 2 was used instead. Due to the relatively small magnitude signal that the Analog Discovery 2 can produce, a power amplifier was used to boost the signal. Sections 6.2.1 and 6.2.2 detail how the ultrasound transducer assembly was constructed and tested.

6.2.1 Transducer Assembly Construction

The first step in constructing the transducer rings was to verify the positive and negative terminals of each transducer. This is an important step because if all the

transducers are not wired in the same orientation, the waves they emit could cause destructive interference and "cancel out" the wave. To perform this verification one transducer was selected as the "true" orientation and each other transducer was compared to it one at a time. Using the breadboard set up shown in Figure 6.8, both the true and test transducers were powered with a 1.6 V_{PP}, 40 kHz signal.

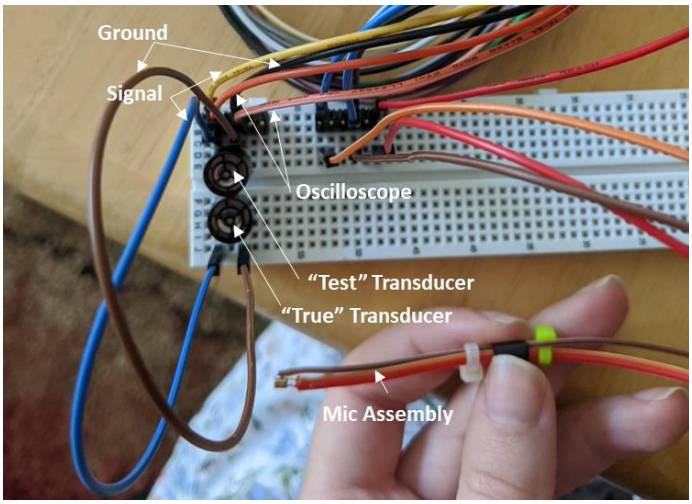

Figure 6.8. Transducer orientation check set-up.

The emitted signal from both transducers was measured using the microphone assembly and compared to the signal of a single transducer. If the transducers were oriented in the same direction, the emitted waves would constructively interfere to create a signal with a larger amplitude than that of the single transducer. If the transducers were not oriented in the same direction, however, the signals would destructively interfere to create a wave with a smaller amplitude. The scope captures shown in Figure 6.9, show the measured emitted signals for a single transducer, constructively interfering transducers, and destructively interfering transducers. The correct orientation with respect to the true transducer was marked on each transducer package.

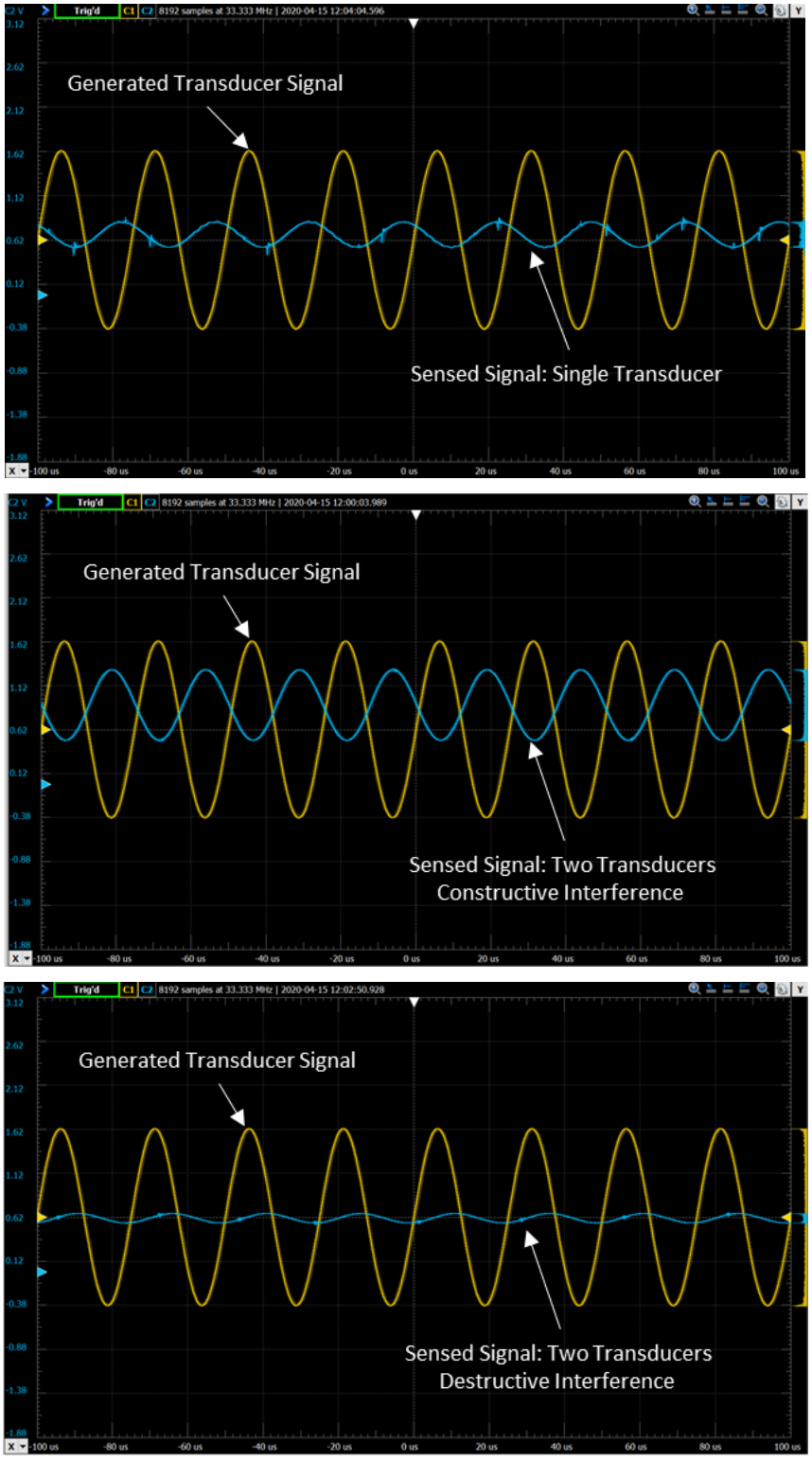

Figure 6.9. Scope captures of generated transducer signal with sensed single transducer signal (Top), sensed constructive interference signal (Middle), and sensed destructive signal (Bottom).

Each of the two transducer rings were constructed according to the circuit diagram shown in Figure 6.10, each with eight transducers connected in parallel.

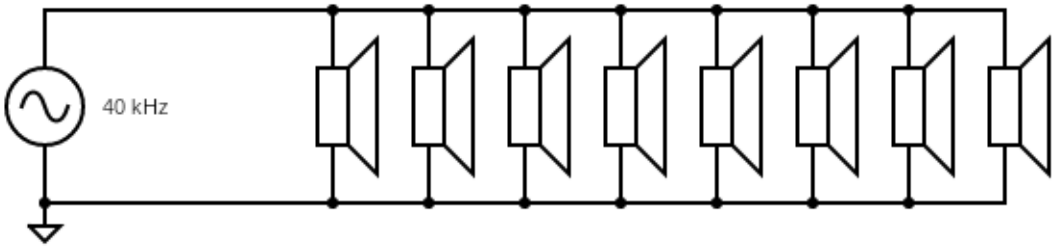

Figure 6.10. Circuit diagram of transducer ring assembly.

To provide structural support for the transducer rings, protoboard rings were cut out of thin flexible protoboard with an inner diameter of ¾ inch. The transducers were then arranged equidistantly around the ring such that all the positive terminals were located around the outside of the ring, and the negative terminals inside. Each positive terminal was soldered to the protoboard. Then, all the negative terminals were connected by soldering 20 AWG solid-core wire between them. The same was done for all the positive terminals. Finally, 18 AWG multicore wire was soldered to each set of terminals. The multicore wire allows for the connection from the transducer ring to the amplifier. This process is shown in Figure 6.11 and was performed two times to create two transducer rings.

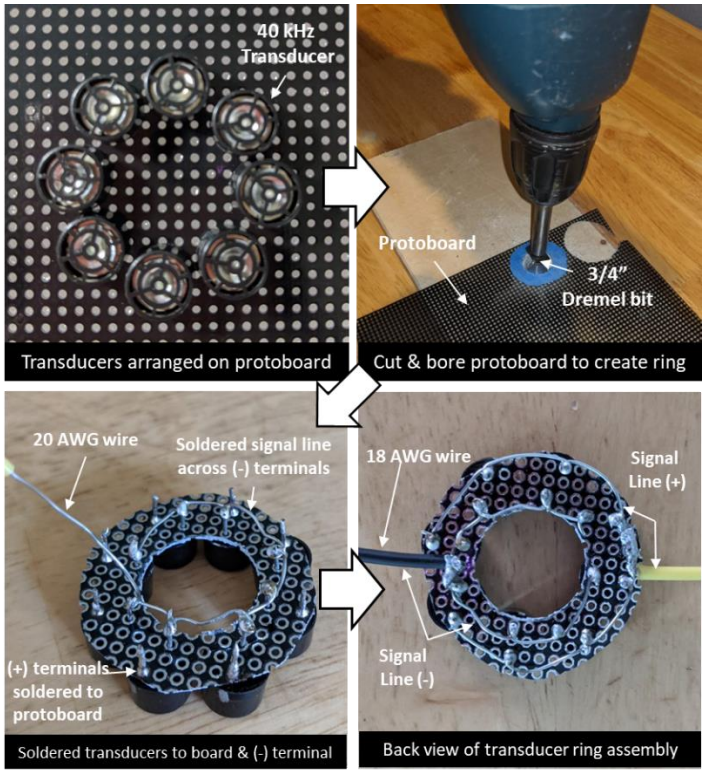

Figure 6.11. Transducer ring construction process.

6.2.2 Transducer Assembly Functionality Check

A functionality check was performed to ensure that the ultrasound transducer rings were producing the expected signal. To perform the check one transducer ring was placed at each end of the copper pipe approximately twelve inches apart. The transducers can be used to both emit and sense a 40 kHz signal through the vibration of their internal membrane. So, the transducer ring on the left was wired to emit a 200 mV_{pp} 40 kHz signal, and the transducer on the right was wired to an oscilloscope to sense the signal emitted by the other set of transducers. This set-up is shown in Figure 6.12, where the transducer ring on the left is labeled "1" and the transducer ring on the left is labeled "2".

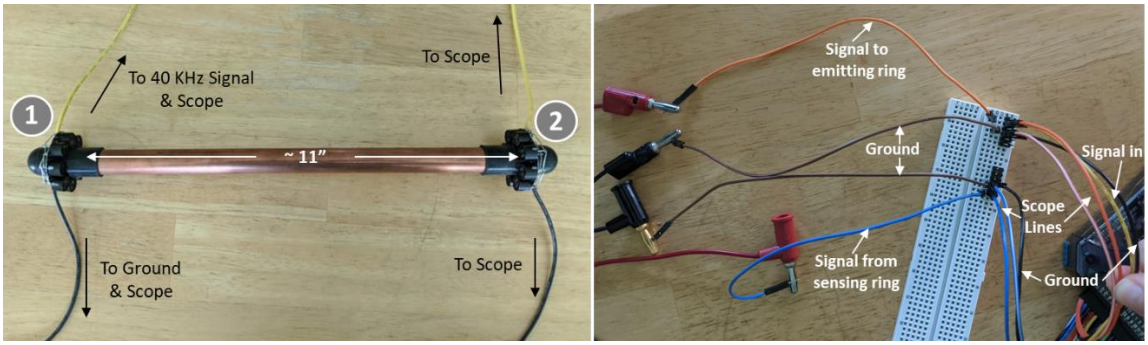

Figure 6.12. Transducer ring check set-up along pipe (Left) and electrical (Right).

The check was performed a second time using the same process but with the transducer ring on the right side (labeled 2) emitting the signal and the transducer ring on the left (labeled 1) sensing. The results from both tests are shown in the oscilloscope captures presented in Figure 6.13.

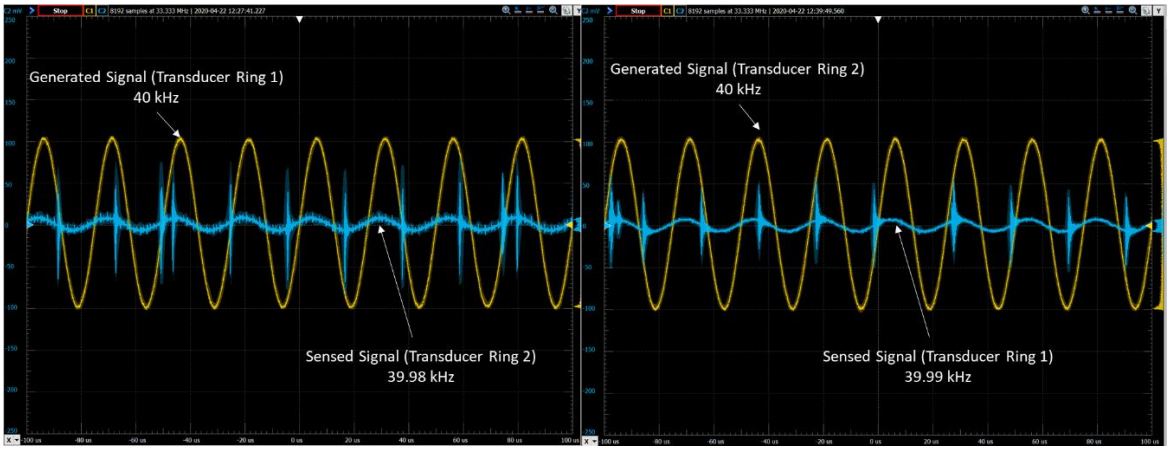

Figure 6.13. Oscilloscope captures of emitted signal from transducer ring 1 and sensed signal from transducer ring 2 (Left), and emitted signal from transducer ring 2 and sensed signal from transducer ring 1 (Right).

As seen in the scope captures, the sensed emitted signal from both transducer ring assemblies was measured to be approximately 40 kHz. This gives us confidence that the transducer rings are producing the appropriate signal frequency and that they are functioning as expected.

6.2.3 Ultrasound Standing Wave Check

The final check performed on the Ultrasound Subsystem was to see if the system could create a standing wave. To properly form a standing wave, the transducer rings must be placed a distance equal to an integer number of wavelengths away from each other [18]. This allows for the wave emitted by each transducer to complete its full wave cycle before being reflected by the opposing transducer ring. When each emitted wave is reflected at the end of its cycle, the chance that the reflected wave will destructively interfere with the emitted wave is decreased. If done properly, the emitted and reflected waves should be in-phase and should create a standing wave.

The wavelength for this check depends on the emitted transducer signal, and can be determined using Equation 2.8 described in Section 2.3 and shown below,

$$c_s = f\lambda. \tag{2.8}$$

Using the speed of sound in room temperature air $c_s = 343\ \mathrm{m/s}$ and the transducer frequency $f = 40\ \mathrm{kHz}$, the wavelength is calculated to be $\lambda = 8.6\ \mathrm{mm}$. Using a ruler, marks were made along a ½ inch diameter pipe every 8.6 mm to indicate the approximate wavelength of the emitted signal. The transducer rings were then placed facing each other with a distance equivalent to 37 wavelengths between them along the pipe as shown in Figure 6.14.

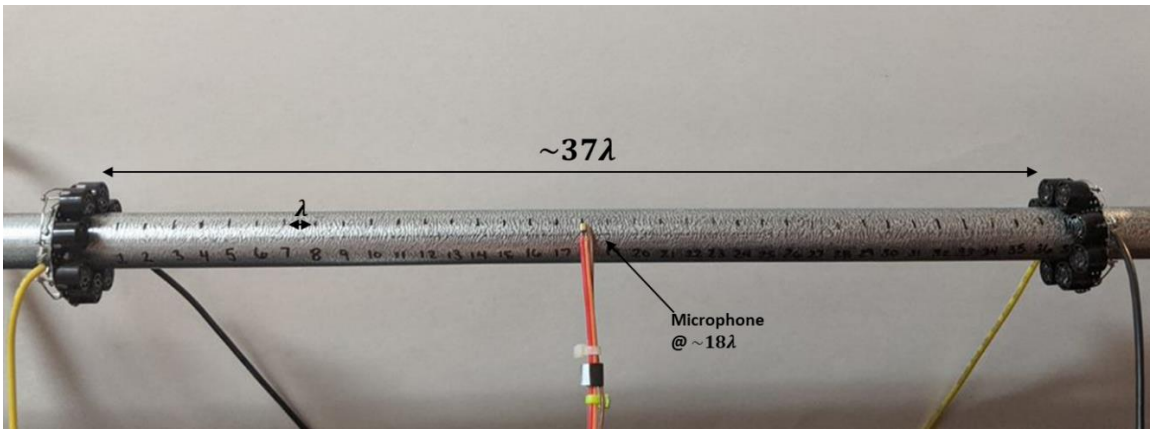

Figure 6.14. Standing wave check set-up.

Both transducer rings were powered using the Analogy Discovery 2's signal generator at 2 V_{pp} and a 40 kHz frequency. The wave created was assessed along a single wavelength, using the microphone assembly. Figure 6.15 shown on the next page presents scope captures of the microphone readings at the beginning, one-fourth, one-half, three-fourths, and at the end of the 18th wavelength. The figure shows that the magnitude of the wave varies significantly along the wavelength. The maximum readings are seen at the beginning, half-way point, and end of the wavelength with the magnitude measuring 294.27 mV_{RMS}, 308.30 mV_{RMS}, and 392.80 mV_{RMS}, respectively. The minimum readings are seen at the one-fourth and three-fourths of a wavelength with the magnitude measuring 180.43 mV_{RMS} and 145.89 mV_{RMS}. These large attenuations in signal are indicative of a standing wave and give us confidence that the system can create a standing wave.

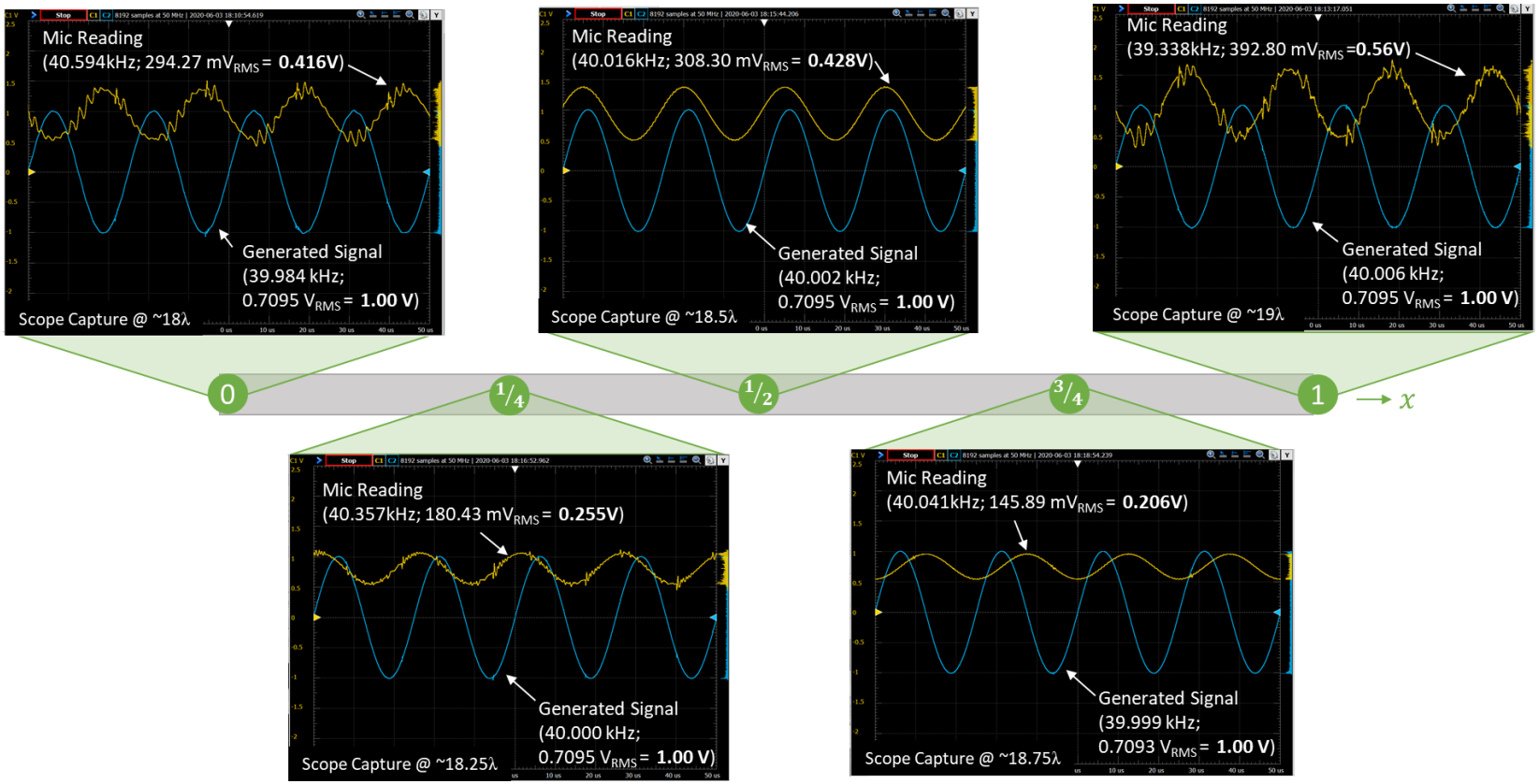

Figure 6.15. Standing wave verification scope captures along the 18th wavelength.

Chapter 7

40 kHz EXPERIMENT RESULTS AND DISCUSSION

An experiment was performed to investigate the effects of a 40 kHz standing ultrasound wave on natural convection from a horizontal cylinder. The experiment used the apparatus shown in Figure 7.1 and detailed in Chapters 3 through 6.

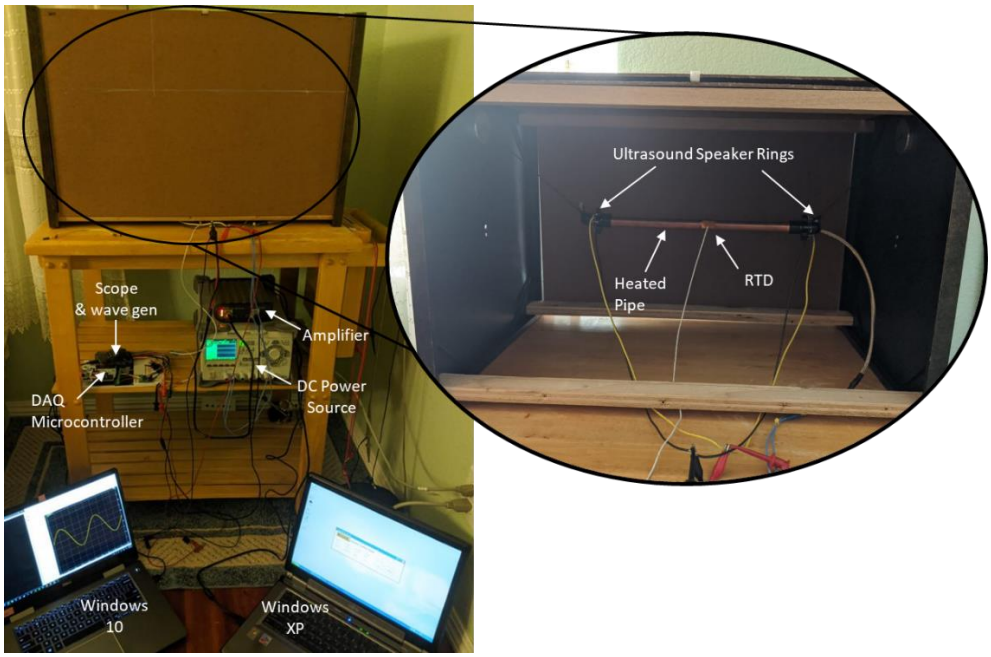

Figure 7.1. Experimental apparatus for 40 kHz ultrasound wave.

In the following sections the experimental process and conditions are detailed. Additionally, the experimental results are presented and discussed. Section 7.1 discusses the findings of the experiment conducted with the shiny finish pipe and data collected with the RTD assembly. Section 7.2 discusses the experiment conducted with the matte black finish pipe and data collected with both the thermal camera and the RTD assembly. Finally, Section 7.3 presents the *Smoke Visualization Test* performed to check if there is a boundary layer perturbance.

7.1 40 kHz Experiment

The goal of the experiment is to see if the system has a measurable response to the actuation of air surrounding the pipe with a 40 kHz standing wave. This experiment was conducted in San Luis Obispo over the course of approximately one and a half hours. The shiny finish metal pipe was used so radiation heat transfer could be considered negligible. Temperature data was taken continuously from the pipe surface with the RTD assembly. Ambient temperature was recorded from the thermo-hygrometer probe to be 26°C, and the power into the system was 14.81 W read from the power supply. The ultrasound transducer rings were located approximately 37 wavelengths away from each other and were powered by the Analog Discovery 2 and amplifier assembly with a 40 kHz 10 V_{pp} signal. The experiment was conducted with the enclosure door closed to reduce the impact of the external environment on the ambient air. The experimental set-up inside the enclosure can be seen in Figure 7.2.

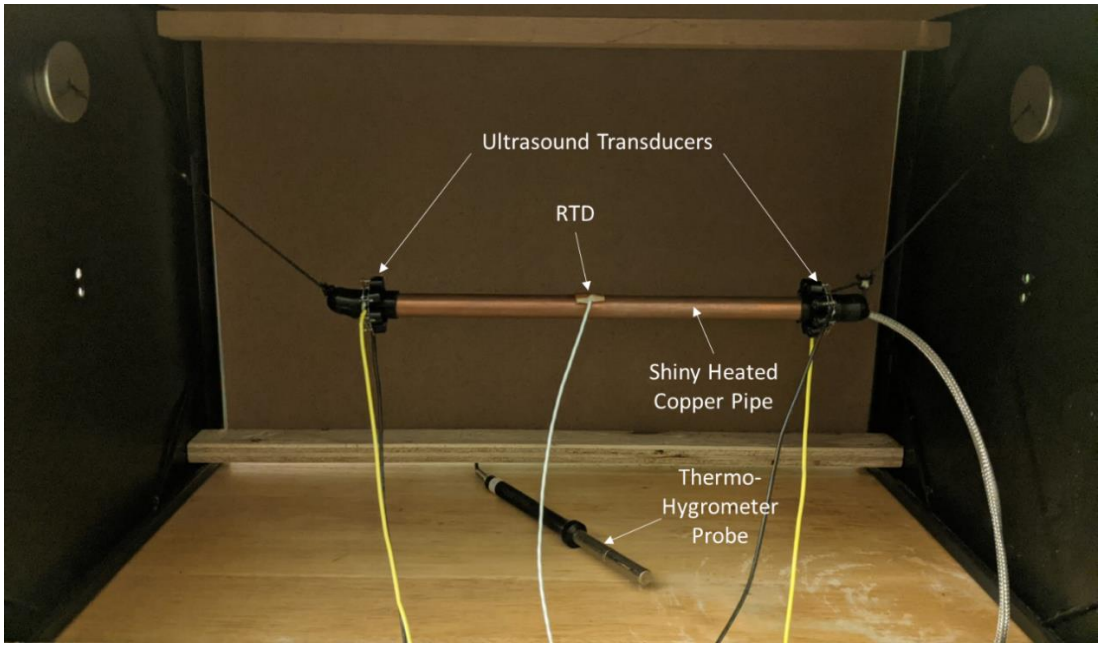

Figure 7.2. Set-up for 40 kHz experiment with shiny pipe finish.

During the test, the system was first allowed to reach its steady state condition before the ultrasound transducer rings were powered. After steady state was reached, the transducers were simultaneously turned on to create a standing wave. The typical response of the system is graphed in Figure 7.3, where the vertical dashed line represents the time at which the ultrasound transducers were powered on.

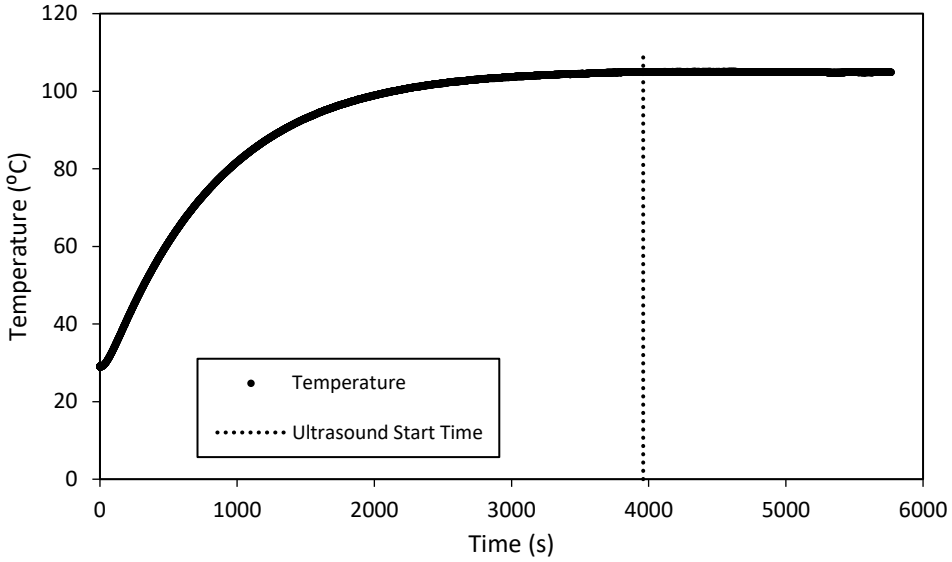

Figure 7.3. Plot of surface temperature response to standing 40 kHz ultrasonic wave.

As shown in the response plotted in Figure 7.3, the steady state surface temperature does not appear to be measurably affected by the ultrasonic wave. Figure 7.4 shows a zoomed-in graph of the surface temperature shortly before and after the start time of the ultrasound wave. Here too, little difference is seen between the steady-state surface temperature measured before and after the ultrasonic actuation. The average temperature reading taken before the ultrasound wave (from 3500 – 3960 seconds) is 104.80℃ ± 0.15℃, and the average temperature reading during the ultrasonic actuation (from 3961 –

5755 seconds) is 104.97°C ± 0.15°C. This indicates that there is no measurable difference in the surface temperature of the pipe with and without a 40kHz standing wave.

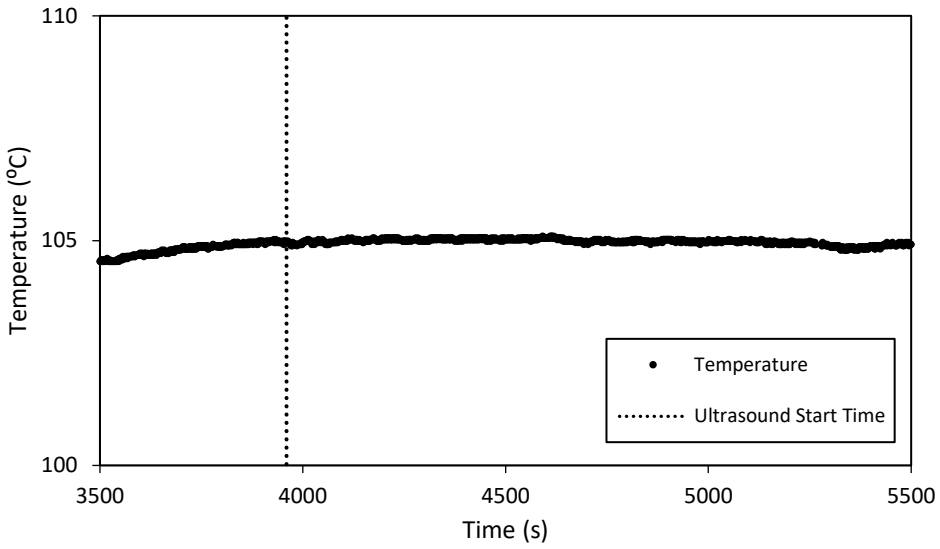

Figure 7.4. Plot of surface temperature response to standing 40 kHz ultrasonic wave from 3500 seconds to 5500 seconds.

Additional runs of the experiment were performed to investigate if activating the ultrasound signal prior to the system reaching steady state would impact the response. Figures 7.5 and 7.6 show the typical system response to ultrasound wave activation at 2000 seconds and 3000 seconds, respectively. For both runs the ambient temperature was 26°C, and the power into the system was 14.64 W.

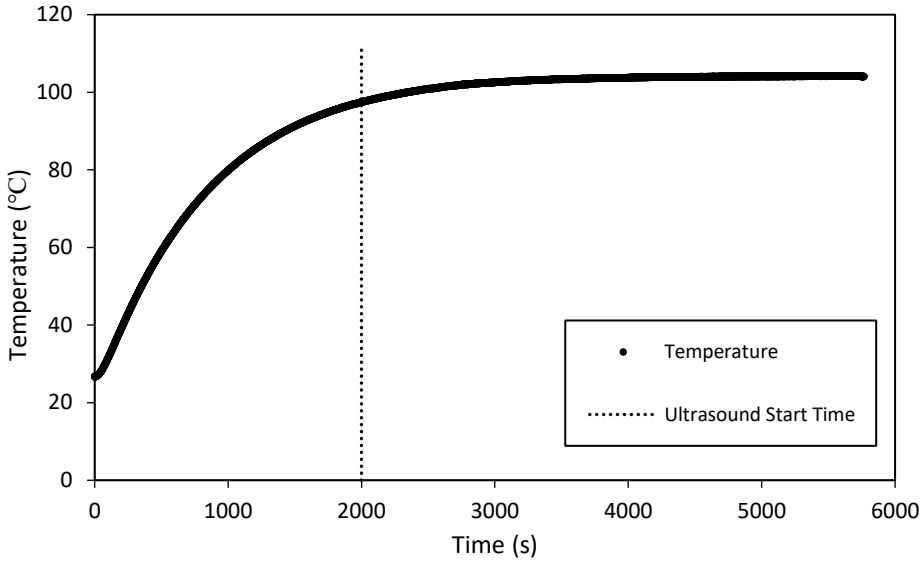

Figure 7.5. Plot of surface temperature response to standing 40 kHz ultrasonic wave activated at 2000 seconds.

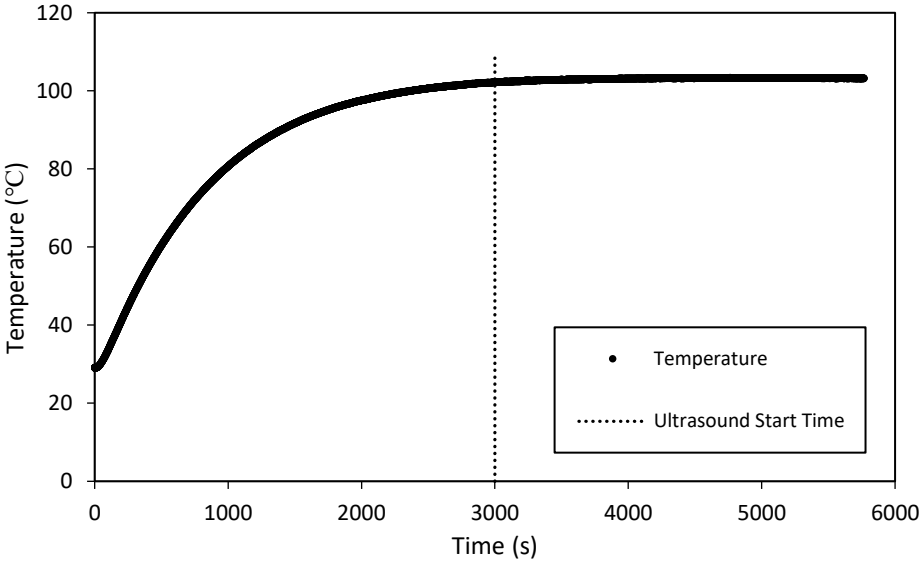

Figure 7.6. Plot of surface temperature response to standing 40 kHz ultrasonic wave activated at 3000 seconds.

The plots presented in Figures 7.5 and 7.6 do not show any apparent cooling effect resulting from the standing 40 kHz ultrasound wave. From the data presented in Figures

7.3 through 7.6 it appears that there is no measurable global enhancement in cooling when a 40 kHz standing ultrasound wave is applied to a heated horizontal cylinder.

Based on the literature review presented in Section 1.1, we saw that a 40 kHz signal has a measurable effect on the heat transfer in water. However, in this experiment we did not see a measurable impact on heat transfer in air. The reason we are not seeing this effect could be due to the density and compressibility differences between water and air. As discussed in Section 2.3, the wavelength of an acoustic wave depends, in part, on the density of the media that it is propagating through. This is because the wavelength is dependent on the speed of sound, which, in turn, depends on the density of the medium it is propagating through. Therefore, a 40 kHz signal in air has a different wavelength than it does in water, making it a fundamentally different wave in each medium. Additionally, water under normal conditions is considered incompressible, whereas air is a compressible fluid. Because acoustic waves are essentially pressure waves, the difference in compressibility between water and air could mean that objects experiencing sound waves in water experience a stronger coupling to the transducer. For these reasons, 40 kHz may not produce the same results in air as it does in water.

7.2 40 kHz Experiment Thermal Imaging

The RTD assembly only collects data at one point on the pipe and as such is not equipped to capture different temperatures along the pipe. The goal of the test is to see if there are any localized temperature variations along the heated pipe caused that were not captured by the RTD assembly. This experiment was conducted in San Luis Obispo over the course of approximately three and a half hours. Temperature data was taken

continuously from the pipe surface with the RTD assembly and thermal images were taken using the FLIR C5 Thermal Camera. The matte black finish copper pipe was used so that it could be properly captured by the thermal camera. Ambient temperature was recorded from the thermo-hygrometer probe to be 20℃, and the power into the system was 14.84 W read from the power supply. The ultrasound transducer rings were located approximately 37 wavelengths away from each other and were powered by the Analog Discovery 2 and amplifier assembly with a 40 kHz 10 V_{pp} signal. The experiment was conducted with the enclosure door open to allow for the capture of thermal images. The experimental set-up inside the enclosure can be seen in Figure 7.7.

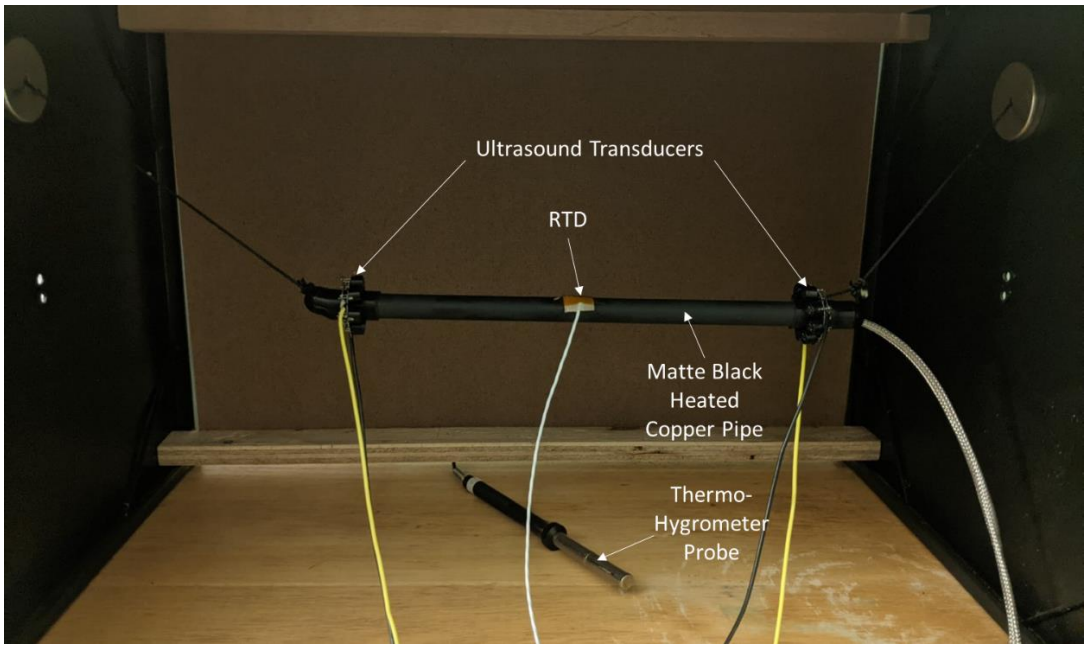

Figure 7.7. Set-up for 40 kHz experiment with matte black pipe finish.

During the test, the system was first allowed to reach its steady state condition before the ultrasound transducer rings were powered. After steady state was reached, a thermal image was taken. Then, the transducers were simultaneously turned on to create a standing wave. After approximately 11791 seconds from the start of the experiment, another thermal

image was captured. The thermal images for before and during the ultrasonic actuation are shown in Figure 7.8.

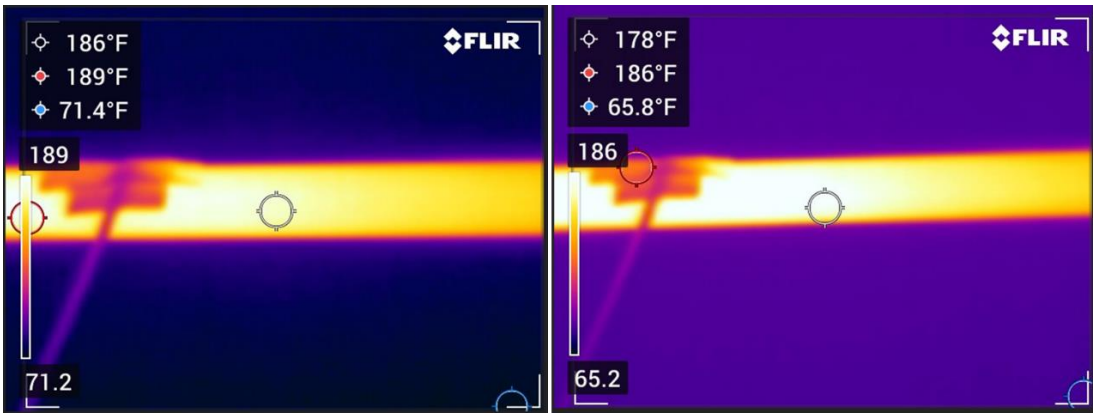

Figure 7.8. Thermal images of heated pipe without ultrasonic wave (Left) and with ultrasonic wave (Right).

The thermal images presented in Figure 7.8 appear to indicate an overall drop in temperature across the entire image with ultrasonic actuation as compared to without. At the location of interest (indicated by the center cross hairs) the temperature reading without and with the ultrasonic wave is 186°F (85.6°C) and 178°F (81.1°C), respectively. A drop in temperature is also shown in the minimum and maximum temperature values between the without and with ultrasound conditions. The maximum temperature recorded is 189°F (87.2°C) and 186°F (85.6°C) for without and with ultrasound, respectively. The minimum temperature recorded is 71.4°F (21.9°C) and 65.8°F (18.78°C) for without and with ultrasound, respectively. These differences, however, are not supported by the temperature data collected by the RTD over the same time. The temperature response of the system captured by the RTD assembly is graphed in Figure 7.9, where the vertical dashed line represents the time at which the ultrasound transducers were powered on.

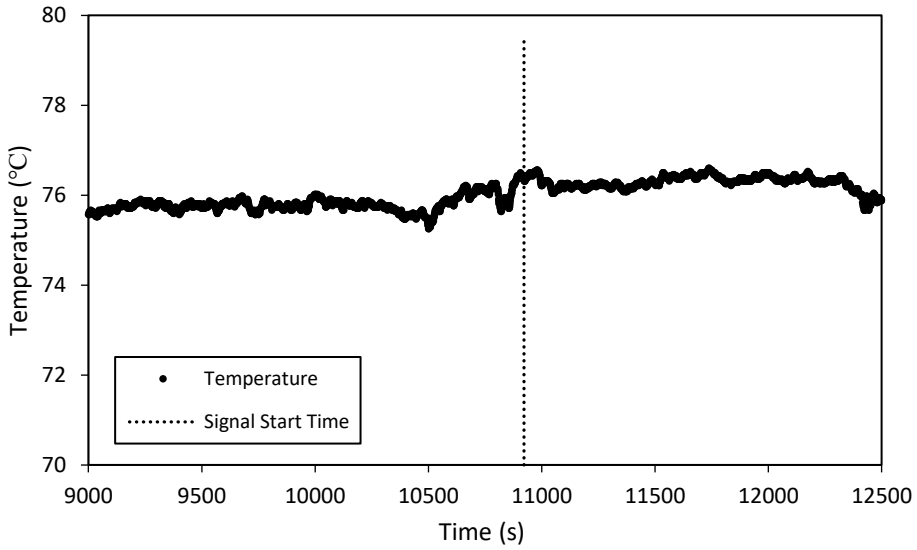

Figure 7.9. Plot of surface temperature response to standing 40 kHz wave with matte black pipe finish.

Despite the temperature values obtained from the thermal images, the RTD data presented in Figure 7.9 does not support a significant change in surface temperature without and with the ultrasound wave activated. The data shows that for the period before the ultrasound activation (from 9000 to 10922 seconds) the minimum, average, and maximum temperature readings were 75.26°C ± 0.15°C, 75.80°C ± 0.15°C, and 76.50°C ± 0.15°C, respectively. For the period during the ultrasound wave (from 10923 to 12500 seconds) the minimum, average, and maximum temperature readings were 75.67°C ± 0.15°C, 76.29°C ± 0.15°C, and 76.60°C ± 0.15°C, respectively. This suggests that the measurable temperature difference shown in the thermal images is likely artificial and due to the way each image was taken. As discussed in Section 4.2, obtaining an accurate reading with a thermal camera can be difficult. A change in horizontal distance between the pipe and the camera, a change in the angle at which an image is taken, or a difference in the vertical alignment of the camera can all result in inaccurate temperature readings between

images. In this case, the variance in temperature is likely due to a variance in the orientation of the thermal camera when each image was taken. As such, the thermal camera is only used for qualitative observations between images and to compare relative temperatures within a single image.

An additional thermal image, shown in Figure 7.10, was taken of the entire heated pipe while the transducer rings were powered with a 40 kHz 10 V_{pp} signal to see if there are visible localized temperature differences along the length of the pipe. The RTD assembly was not attached to the pipe for the image. This is to eliminate any impact the RTD assembly has on the boundary layer or the ultrasound wave form, and to reduce the number of objects with differing emissivity in the thermal camera's line of sight. The ambient temperature was 21℃, and the power into the system was 14.84 W.

Figure 7.10. Thermal image of entire heated pipe with 40 kHz standing wave.

From the thermal image shown in Figure 7.10, there does not appear to be a localized temperature difference along the pipe that corresponds to the variance in pressure produced by the standing wave. It should be noted that the lack of visible thermal gradients could be due to the high thermal conductivity and diffusivity of copper. These properties allow the copper pipe to distribute significant quantities of heat quickly and may be overpowering any local affects caused by the ultrasound. Ultimately, however, Figures 7.8 through 7.10 show no visible localized enhancement in cooling when a 40 kHz standing ultrasound wave is applied to a heated horizontal cylinder.

7.3 Smoke Visualization Test

The goal of the Smoke Visualization Test is to visually examine if a 40 kHz standing wave causes a perturbance of smoke within the heated pipe's boundary layer. An incense cone was lit and placed under the pipe to provide smoke and an LED light was placed behind the pipe to illuminate the smoke. Images were taken with a Google Pixel 2 phone camera. The ambient temperature was recorded from the thermo-hygrometer probe to be 22°C, and the power into the system was 14.67 W read from the power supply. The shiny finish copper pipe was used to reduce radiation from the pipe surface. The ultrasound transducer rings were located approximately 37 wavelengths away from each other and were powered by the Analog Discovery 2 and amplifier assembly with a 40 kHz 10 V_{pp} signal. The experiment was conducted with the enclosure door open to allow for the capture of images. The experimental set-up inside the enclosure can be seen in Figure 7.11.

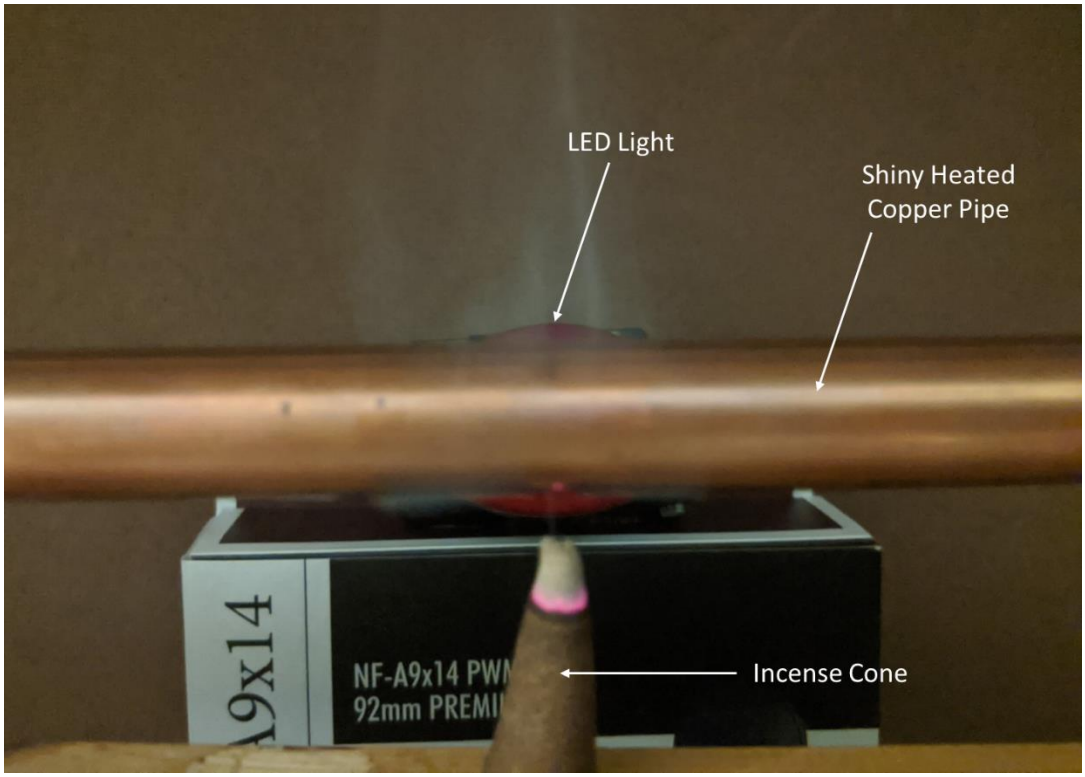

Figure 7.11. Set-up for Smoke Visualization Test.

During the test, the system was first allowed to reach its steady state condition before the incense cone was lit. A picture was then taken of the smoke without the presence of ultrasound. Then, the transducers were simultaneously turned on to create a standing wave and a picture of the smoke was taken. Figure 7.12 shows the images of the smoke without and with the presence of the standing wave.

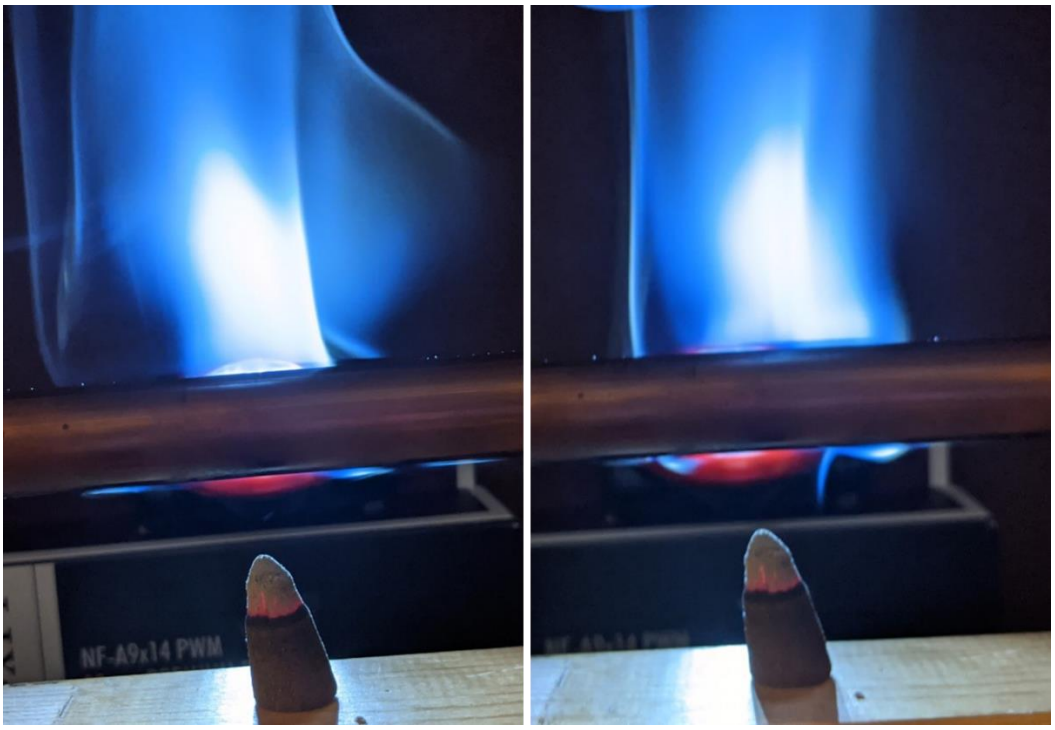

Figure 7.12. Smoke test without 40 kHz standing wave (Left) and with 40 kHz standing wave (Right).

When comparing the images shown in Figure 7.12 there does not appear to be a visible perturbance of the smoke when a 40 kHz standing wave is applied. This observation leads us to conclude that the 40 kHz standing wave may not be perturbing the boundary layer created by the cylinder in natural convection.

Chapter 8

200 Hz EXPERIMENTAL RESULTS AND DISCUSSION

Although our experiment showed no measurable effect on heat transfer when a 40 kHz wave was applied, we decided to examine other frequencies. This was of particular interest, because the 40 kHz frequency was selected based on experiments conducted in water and different frequencies may be more appropriate for an air media. So, additional experiments were performed to see if other acoustic frequencies could affect natural convection heat transfer in air. Section 8.1 details the experimental procedure and results of a *Smoke Visualization Test* for acoustic frequencies of 200 Hz, 300 Hz, 400 Hz, 500 Hz, and 2,000 Hz. Section 8.2 describes the experiment performed to investigate if a 200 Hz wave can alter natural convection heat transfer from a heated horizontal pipe.

8.1 Smoke Visualization Test at Various Frequencies

After the Smoke Visualization Test was performed for a 40 kHz wave and the smoke was not visibly perturbed as discussed in Section 7.3, we decided to investigate if other acoustic frequencies could perturb smoke. The goal of the Smoke Visualization Test at Various Frequencies is to visually examine if acoustic waves at 200 Hz, 300 Hz, 400 Hz, 500 Hz, and 2,000 Hz can perturb a plume of smoke. This experiment was conducted using an incense cone to produce smoke and an LED light to illuminate the smoke. The acoustic waves were generated by an Anker Sound Core 2 Bluetooth speaker connected to a Google Pixel 2 cell phone running a frequency generator application. Images were also taken using the Google Pixel 2's phone camera. The experimental set-up is shown in Figure 8.1.

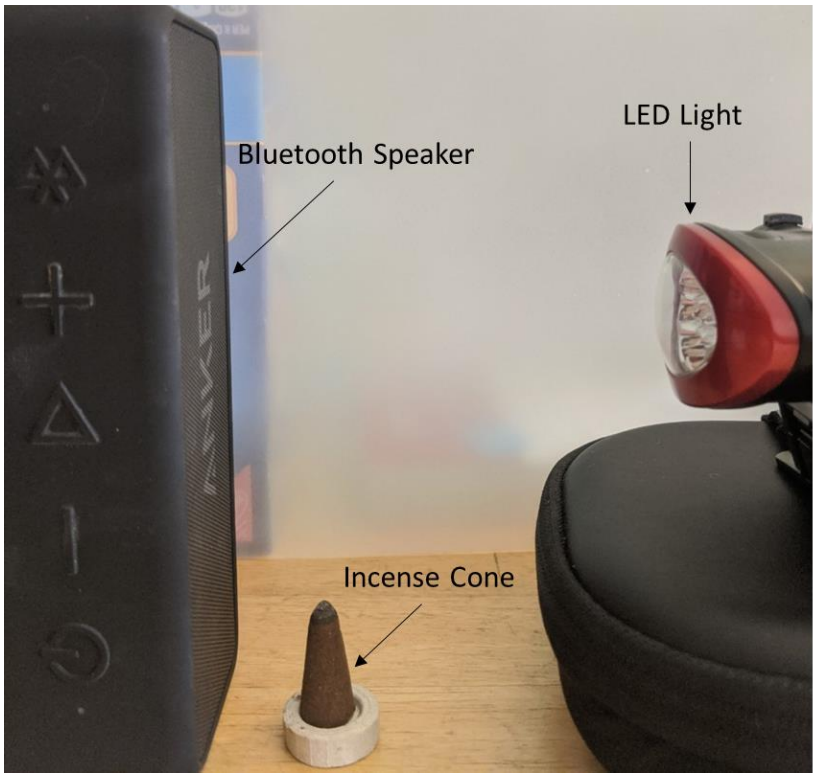

Figure 8.1. Set-up for Smoke Visualization Test at Various Frequencies.

This experiment was run five times, each time at a different frequency. First, the incense cone was lit to create a plume of smoke and the LED light was turned on to illuminate the smoke. Then, the Bluetooth speaker was turned on to the highest volume setting equivalent to 85 dB SPL and the desired frequency was generated. Images of the smoke plume were captured at various distances away from the speaker, measured using a ruler. Figures 8.2 through 8.6 show the impact of the acoustic wave on the smoke plume for the frequencies of 200 Hz, 300 Hz, 400 Hz, 500 Hz, and 2,000 Hz, respectively.

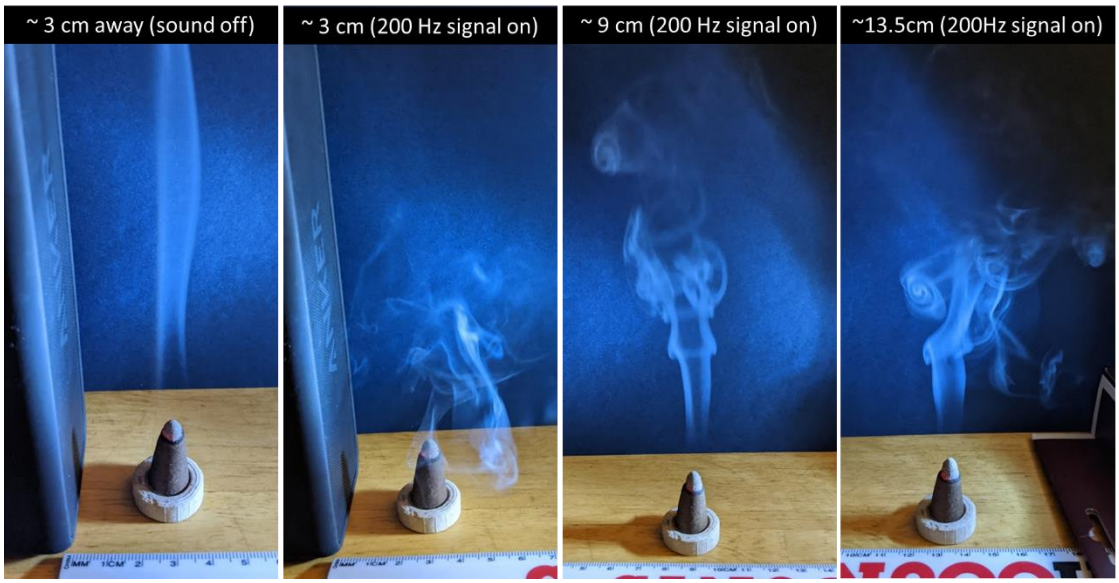

Figure 8.2. Smoke plume response to 200 Hz acoustic wave at approximately 3cm, 9cm, and 13.5cm away from the speaker compared to smoke plume in the absence of the acoustic wave (Left).

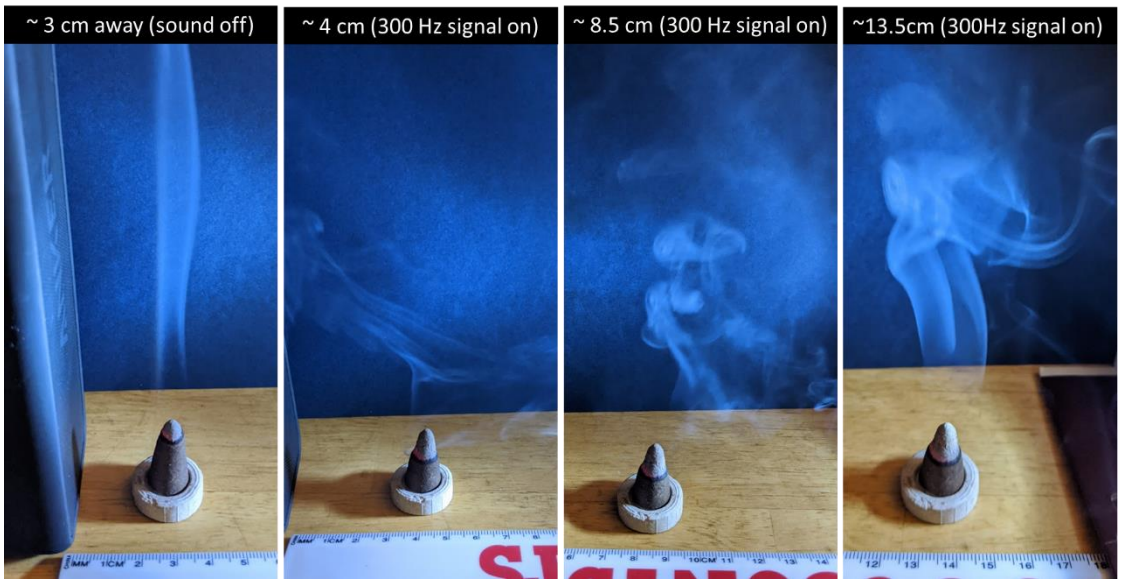

Figure 8.3. Smoke plume response to 300 Hz acoustic wave at approximately 4cm, 8.5cm, and 13.5cm away from the speaker compared to smoke plume in the absence of the acoustic wave (Left).

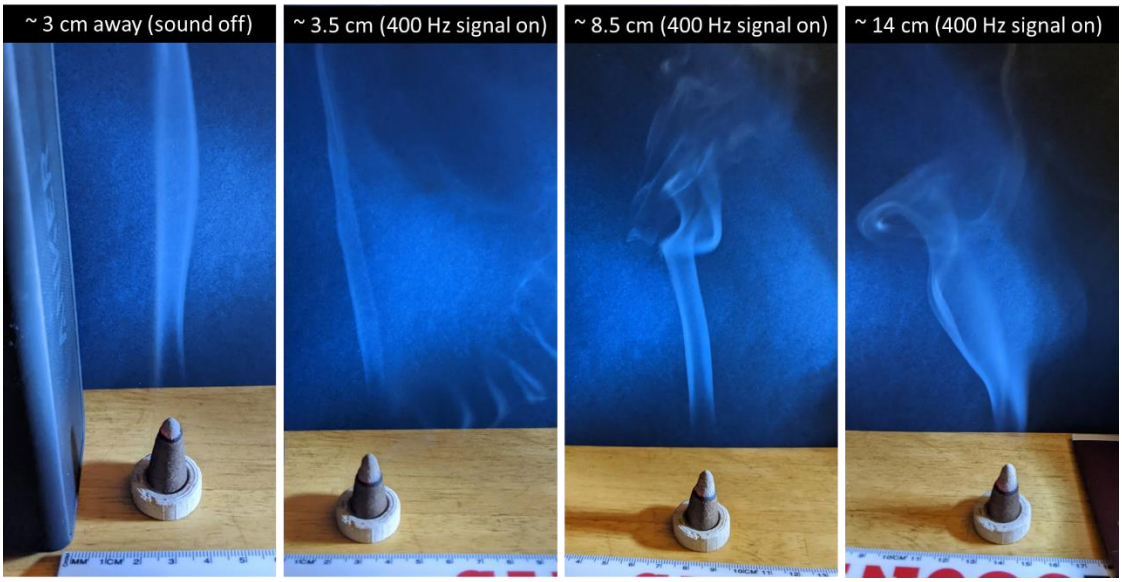

Figure 8.4. Smoke plume response to 400 Hz acoustic wave at approximately 3.5cm, 8.5cm, and 14cm away from the speaker compared to smoke plume in the absence of the acoustic wave (Left).

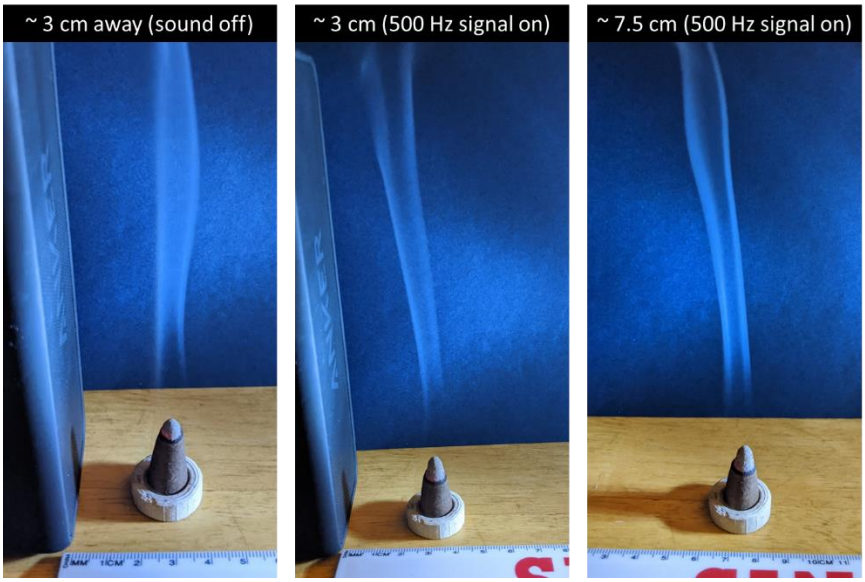

Figure 8.5. Smoke plume response to 500 Hz acoustic wave at approximately 3cm and 7.5cm away from the speaker compared to smoke plume in the absence of the acoustic wave (Left).

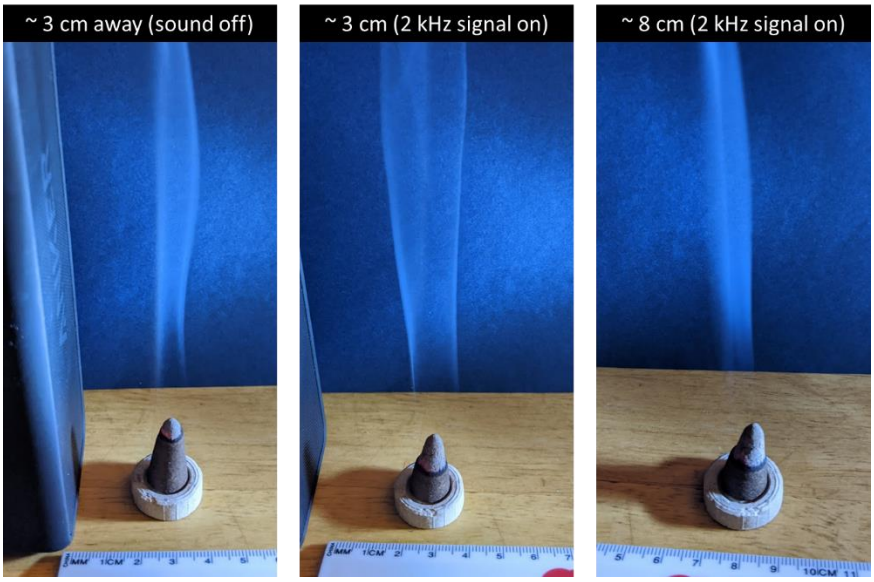

Figure 8.6. Smoke plume response to 2,000 Hz acoustic wave at approximately 3cm and 8cm away from the speaker compared to smoke plume in the absence of the acoustic wave (Left).

Figures 8.2 and 8.3 show the smoke plume response to 200 Hz and 300 Hz acoustic waves, respectively. In both the cases the plume was greatly perturbed by the signal, creating visibly turbulent flow at all the tested distances away from the speaker. This indicates that an acoustic wave can affect a flow regime in air. Figure 8.4 shows the smoke plume response to a 400 Hz signal. The plume under this condition was also visibly perturbed at all the tested locations, but not as drastically as with the 200 Hz and 300 Hz acoustic waves. The smoke plume, however, was not visibly disturbed in the 500 Hz and 2,000 Hz test cases. The apparent decrease in the impact of the 400 Hz acoustic wave on the plume and the apparent absence of an effect on the plume at 500 Hz and 2,000 Hz, indicates that only certain frequencies of acoustic wave can impact a flow regime in air. Based on this observation, we decided to investigate the effects of a 200 Hz wave on the

heated horizontal cylinder experimental apparatus. This is discussed in further detail in Section 8.2.

8.2 200 Hz Experiment

Since a 200Hz acoustic wave was found to affect the flow of a smoke plume (as shown in Section 8.1), we wanted to see if it could affect heat transfer. The goal of this experiment is to see if the heated horizontal cylinder system has a measurable response to the actuation of air surrounding the pipe with a 200 Hz wave. This experiment was conducted in San Luis Obispo over the course of approximately two hours. The shiny finish metal pipe was used so radiation heat transfer could be considered negligible. Temperature data was taken continuously from the pipe surface with the RTD assembly. Ambient temperature was recorded from the thermo-hygrometer probe to be 19℃, and the power into the system was 14.59 W read from the power supply. The 200 Hz acoustic wave was generated by an Anker Sound Core 2 Bluetooth speaker placed below the pipe. The speaker was connected to a Google Pixel 2 cell phone running a frequency generator application. The experiment was conducted with the enclosure door closed to reduce the impact of the external environment on the ambient air. The experimental set-up inside the enclosure can be seen in Figure 8.7.

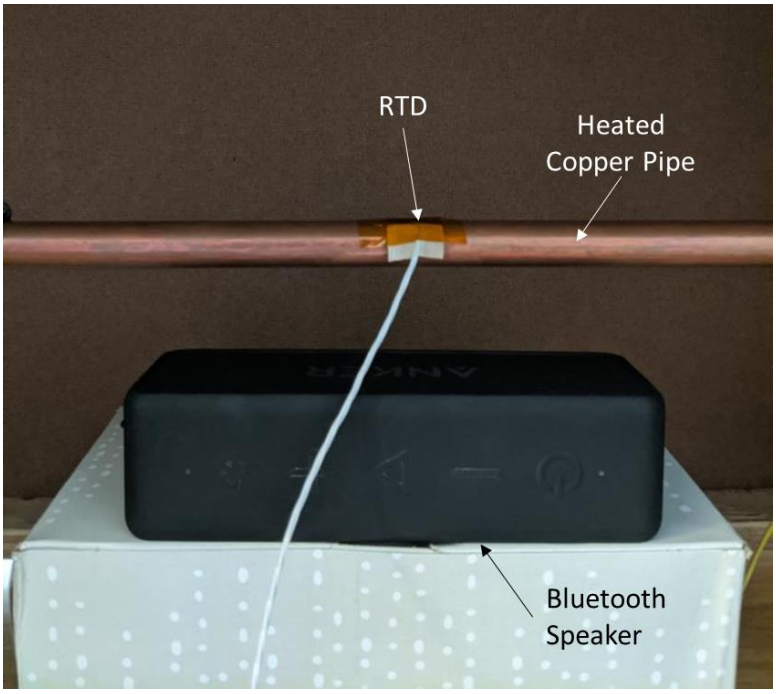

Figure 8.7. Set-up for 200 Hz experiment with shiny pipe finish.

During the test, the system was first allowed to reach its steady state condition before the speaker was activated to produce a 200 Hz signal at full volume (approximately 85 dB SPL). The typical response of the system is graphed in Figure 8.8, where the vertical dashed line represents the time at which the 200 Hz signal was started.

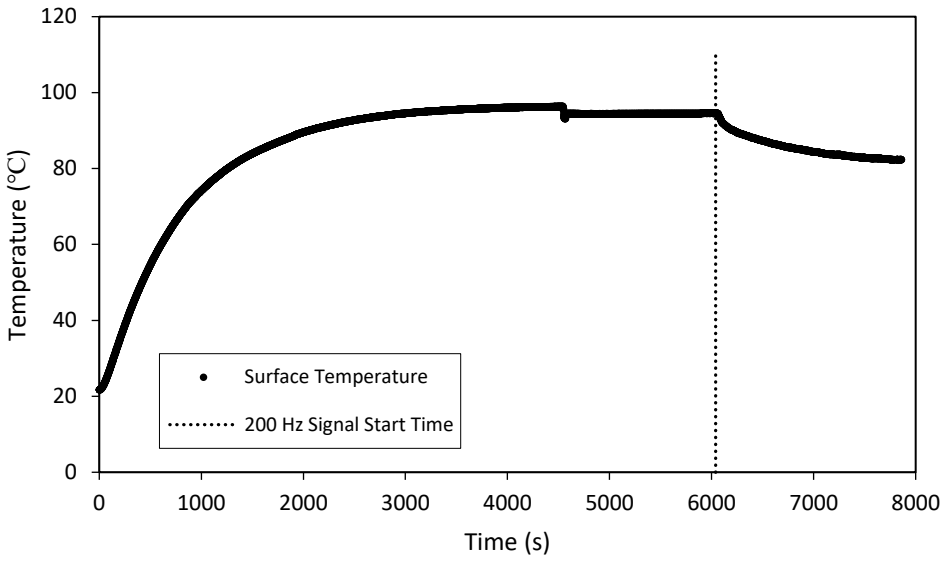

Figure 8.8. Plot of surface temperature response to 200 Hz acoustic wave.

As shown in the response plotted in Figure 8.8, there is a significant reduction in the steady state surface temperature after the 200 Hz wave is activated. It should be noted that the recorded fluctuation in the temperature at approximately 4587 seconds is due to the enclosure door being lifted to adjust the speaker. The system was then allowed to settle to a steady state temperature before the 200 Hz signal was started. Figure 8.9 shows a zoomed in graph of the surface temperature shortly before and after the start time of the acoustic wave.

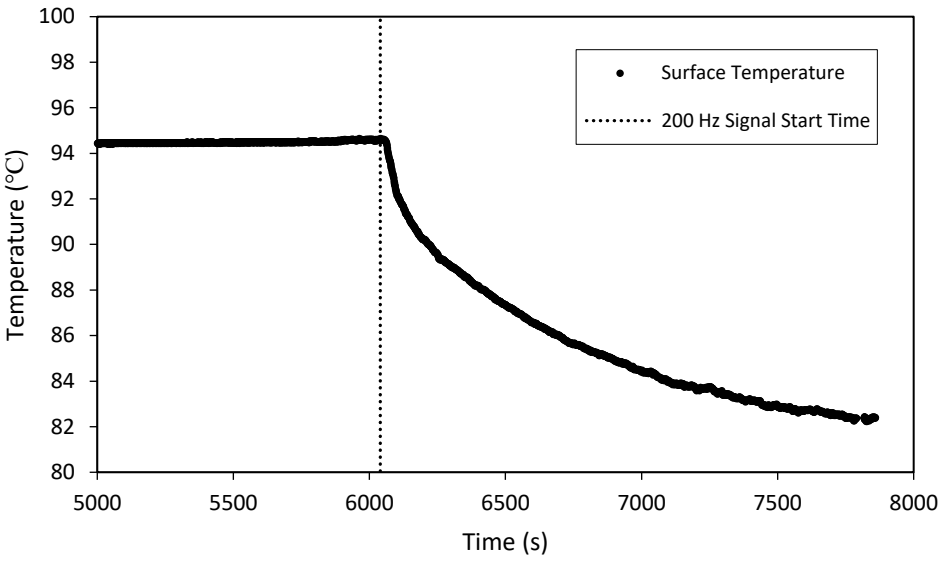

Figure 8.9. Plot of surface temperature response to 200 Hz acoustic wave from 4600 seconds to 7858 seconds.

Based on the data presented in Figure 8.9, the average temperature reading taken before the 200 Hz wave (from 4600 – 6040 seconds) was 94.49℃ ± 0.15℃, and the lowest recorded temperature reading during the acoustic actuation was 82.24℃ ± 0.15℃. This 12.25℃ decrease in the steady state temperature indicates a measurable difference in the surface temperature of the pipe without and with a 200 Hz wave. Furthermore, the heat transfer coefficient was calculated to be $h = 10.92\ \mathrm{W/m^2K}$ without acoustic actuation and $h = 13.04\ \mathrm{W/m^2K}$ with. This 19.4% difference in heat transfer coefficients supports the concept that a 200 Hz acoustic wave can enhance cooling in natural convection heat transfer.

It is interesting that a 200 Hz acoustic wave has a significant measurable impact on natural convection heat transfer in air, but a 40 kHz signal does not. The fundamental difference between the 40 kHz and 200 Hz waves is their wavelength. A 40 kHz signal has an 8.6 mm wavelength in room temperature air whereas the wavelength of a 200 Hz signal

is 1500 mm. The wavelength in relation the dimensions of the heated object may therefore play a role in the impact the wave has on heat transfer enhancement. The length of the pipe is over 30x the wavelength of the 40 kHz signal but only about a fifth the length of the 200 Hz signal wavelength. It is possible that the size of the experimental apparatus was optimal for heat transfer enhancement with a 200 Hz signal but for a 40 kHz signal.

The mechanism behind the apparent heat transfer enchainment with a 200 Hz wave is not well understood. However, we do not believe it is due to the speaker creating a forced convection regime as a fan would. This can be justified by calculating the air particle displacement caused by acoustic waves using the method described by Valière [20]. Per the calculation performed in Appendix B, a 200 Hz, 85 dB wave results in an air particle displacement magnitude of only 0.99 μm. This indicates that the wave itself is not creating bulk fluid motion as you would see in forced convection.

We would speculate that the phenomenon that causes the cooling enhancement is a standing wave-like effect which is known to occur in the "very near field" of speakers. The very near field exists in the space immediately next to the face of the speaker and extends only a fraction of the wavelength away from the face. In this region, a pressure null can occur for certain frequencies [21]. This drastic variance in pressure could be the cause of the observed heat transfer enhancement as the heated pipe was within the ultra near field of the 200 Hz wave.

Chapter 9

CONCLUSIONS AND FUTURE WORK

9.1 Summary and Conclusions

In this thesis we explored the impact of acoustic waves on natural convection heat transfer from a horizontal cylinder in air. The cylinder geometry was approximated by a heated Type-M copper pipe with a nominal diameter of 1/2 inches and a length of 12 inches. Two ultrasonic transducer ring assemblies, operating at 40 kHz, were constructed and arranged to create a standing wave along the length of the pipe. Experiments were also performed in the audible range using an Anker Sound Core 2 Speaker at 200 Hz, 300 Hz, 400 Hz, 500 Hz, and 2,000 Hz.

While our expectation was that our results would mirror those found in the literature related to cooling enhancement using ultrasound in water (cited in the body of this thesis), they did not. When a 40 kHz signal was used to actuate the air surrounding the heated cylinder assembly, no measurable enhancement of heat transfer was detected. This could be due to the density and compressibility differences between air and water. The wavelength of an acoustic wave depends, in part, on the density of the media that it is propagating through. Therefore, a 40 kHz signal in air has a different wavelength than it does in water, making it a fundamentally different wave in each medium. Additionally, water under normal conditions is considered incompressible, whereas air is a compressible fluid. Because acoustic waves are essentially pressure waves, the difference in compressibility between water and air could mean that objects experiencing sound waves in water experience a stronger coupling to the transducer. For these reasons, 40 kHz may not produce the same results in air as it does in water.

Interestingly, however, we found that a 200 Hz acoustic wave does have a significant measurable impact on natural convection heat transfer in air. The steady state surface temperature of the pipe dropped by approximately 12℃ when a 200 Hz wave was applied to the system. The fundamental difference between the 40 kHz and 200 Hz waves is their wavelength. A 40 kHz signal has an 8.6 mm wavelength in room temperature air whereas the wavelength of a 200 Hz signal is 1500 mm. The wavelength in relation the dimensions of the heated object may therefore play a role in the impact the wave has on heat transfer enhancement. The length of the pipe is over 30x the wavelength of the 40 kHz signal but only about a fifth the length of the 200 Hz signal wavelength. It is possible that a system with a heated object commensurate with the wavelength of a 40 kHz signal may experience enhanced cooling. We recommend that further investigation into cooling with a 40 kHz frequency be done using smaller objects on the order of 5mm or less.

While we saw the enhancement of heat transfer using a 200 Hz signal, the mechanism behind this phenomenon is not well understood. However, we do not believe it is due to the speaker creating a forced convection regime as a fan would. A 200 Hz, 85 dB wave results in an air particle displacement magnitude of only 0.99 μm, which is not sufficient to generate bulk fluid motion.

We would speculate that the phenomenon that causes the cooling enhancement is a standing wave-like effect which is known to occur in the “very near field” of speakers. In this region, a pressure null can occur for certain frequencies [21]. This drastic variance in pressure could be the cause of the observed heat transfer enhancement as the heated pipe was within the very near field of the 200 Hz wave. Further investigation into the very near field effect is recommended.

9.2 Future Work

We recommend that several pieces of more advanced equipment be used in any additional studies. First, we suggest that a robust and properly calibrated thermal imaging system be used to obtain temperature data. This will eliminate any interference the boundary layer and acoustic waves experience as a result of the RTD assembly. Second, to observe perturbations of the system's boundary layer or visualize acoustic waves a Schlieren may be used. Additionally, in place of the Digilent Analog Discovery 2, we recommend the use of laboratory bench top equipment. Finally, to investigate the cooling of small objects, a high-power laser may be useful for heating the objects remotely.

We suggest that further investigation be done into the very near field effect and its potential impact on the 200 Hz experiment. We believe this may lead to a better understanding of the mechanism behind the enhanced cooling seen. Additionally, a study investigating the effects of ultrasound on the cooling of objects measuring a fraction of the wavelength is recommended. Such a study may further our understanding of which acoustic frequencies can enhance heat transfer.

REFERENCES

[1] Fand, R.M., 1965, "The Influence of Acoustical Vibrations on Heat Transfer by Natural Convection from a Horizontal Cylinder to Water", Journal of Heat Transfer, **87**(5) pp.309-310.

[2] Li, K.W. and Parker, J.D., 1967, "Acoustical Effects on Free Convective Heat Transfer from a Horizontal Wire", Journal of Heat Transfer, **89**(8) pp.277-278.

[3] Wong, S. W. and Chon, W. Y., 1969, "Effects of Ultrasonic Vibrations on Heat Transfer to Liquids by Natural Convection and by Boiling", AIChE Journal, **15**(2), pp.281–288.

[4] Li, D., Chen, Z. and Shi M., 2010, "Effect of Ultrasound on Frost Formation on a Cold Flat Surface in Atmospheric Air Flow", Experimental Thermal and Fluid Science, **34**(8), pp. 1247-1252.

[5] Boziuk, T. R., Smith, M. K. and Glezer, A., 2016, "Enhanced Boiling Heat Transfer on Plain and Featured Surfaces using Acoustic Actuation", International Journal of Heat and Mass Transfer, **108**, pp. 181-190.

[6] Melkumov, U. and Kurbanov, K., 2003, "Use of Ultrasound for Intensification of Heat Transfer Process in Heat Exchangers", *Proc. International Congress of Refrigeration*, Washington, DC, **4**, pp.1–5.

[7] Monnot, A., Boldo, P., Gondrexon, N., and Bontemps, A., 2007, "Enhancement of Cooling Rate by Means of High Frequency Ultrasound", Heat Transfer Engineering, **28**(1), pp.3-8.

[8] Inworn, N. and Chaiworapuek, W., 2018, "On the Thermal Characteristic of a Heating Flat Surface Under Low Frequency Ultrasonic Waves", International Journal of Heat and Mass Transfer, **122**, pp.1153–1161.

[9] Baffigi, F. and Bartoli, C., 2012, "Influence of the Ultrasounds on the Heat Transfer in Single Phase Free Convection and in Saturated Pool Boiling", Experimental Thermal and Fluid Science, **36**, pp.12–21.

[10] Léal, L., Miscevic, M., Lavieille, P., Amokrane, M., Pigache, F., Topin, F., Nogarède, B. and Tadrist, L., 2013, "An Overview of Heat Transfer Enhancement Methods and New Perspectives: Focus on Active Methods using Electroactive Materials", International Journal of Heat and Mass Transfer, **61**, pp. 505-524.

[11] Engelbrecht, H., and Pretorius, L., 1992, "The Effect of Sound on Natural Convection from a Vertical Flat Plate", *Journal of Sound and Vibration*, **158**(2), pp.213-218.

[12] Bergman, T.L., Lavine, A. S., Incropera, F. P. and Dewitt, D. P., 2011, *Fundamentals of Heat and Mass Transfer*, John Wiley & Sons, Jefferson City, MO.

[13] Churchill, S.W., and Chu, H.S., 1975, “Correlating Equations for Laminar and Turbulent Free Convection from a Horizontal Cylinder”, International Journal of Heat and Mass Transfer, **18**(9), pp.1049-1053.

[14] Qureshi, Z.H., and Ahmad, R., 1987, “Natural Convection from a Uniform Heat Flux Horizontal Cylinder at Moderate Rayleigh Numbers”, Numerical Heat Transfer, **11**(2), pp.199-212.

[15] Morgan, V. T., “The Overall Convective Heat Transfer from Smooth Circular Cylinders,” in T. F. Irvine and J. P. Hartnett, Eds., *Advances in Heat Transfer*, Vol. 11, Academic Press, New York, 1975, pp. 199–264.

[16] Ling, S. J., Sanny, J., and Moebs, B., 2020, “17.3: Speed of Sound”, from https://phys.libretexts.org/Bookshelves/University_Physics/Book%3A_University_Physics_(OpenStax)/Map%3A_University_Physics_I_-_Mechanics_Sound_Oscillations_and_Waves_(OpenStax)/17%3A_Sound/17.03%3A_Speed_of_Sound#:~:text=The%20equation%20for%20the%20speed%20of%20sound%20in%20air%20v,s%E2%88%9AT273K.&text=v%3Df%CE%BB.

[17] Dunst, P., Hemsel, T., Bornmann, P., Littmann, W., and Sextro, W., 2020, “Optimization of Ultrasonic Acoustic Standing Wave Systems”, Actuators, **9**(9), pp.1–12.

[18] Ling, S. J., Sanny, J., and Moebs, B., 2020, “16.7: Standing Waves and Resonance”, from https://phys.libretexts.org/Bookshelves/University_Physics/Book%3A_University_Physics_(OpenStax)/Map%3A_University_Physics_I_-_Mechanics_Sound_Oscillations_and_Waves_(OpenStax)/16%3A_Waves/16.07%3A_Standing_Waves_and_Resonance

[19] Kozuka, T., Yasui, K., Tuziuti, T., Towata, A., and Yasuo, I., 2006, “Non-Contact Acoustic Manipulation in Air”, Proc. Symp. Ultrason. Electron., **27**, pp.509–510.

[20] Valière, J., 2014, *Acoustic Particle Velocity Measurements Using Laser: Principles, Signal Processing and Applications*. John Wiley & Sons, London, England, Chap. 1.

[21] Prezelj, J., Lipar, P., Belšak, A., and Čudina, M., 2013, "On Acoustic Very near Field Measurements." Mechanical Systems and Signal Processing, **40**(1), pp. 194-207.

APPENDIX A

Sample Calculations: Theoretical Surface Temperature and Heat Transfer Coefficient based on the Churchill & Chu and Morgan Correlations

This appendix presents a sample calculation for determining the measured heat transfer coefficient, the theoretical surface temperatures, and heat transfer coefficients based on the Churchill and Chu [12] and Morgan [14] correlations.

From the experimental conditions let:

Measured ambient temperature $T_\infty = 26℃$ or 299.15 K.

Measured surface temperature $T_{s_{meas}} = 104.92℃$ or 378.07K .

Pipe outer diameter $D = 0.0159$ m.

Pipe length $L = 0.355$ m.

Power in $Q = 14.82$ W.

Gravitational constant $g = 9.81\ \mathrm{m}/s^2$.

Calculating Measured Heat Transfer Coefficient:

Newton's Law of Cooling presented in Section 2.2 is used to determine the measured heat transfer coefficient (h_{meas}). Starting with equation 2.7:

$$q" = h(T_s - T_\infty), \tag{2.7}$$

we rearrange to solve for h_{meas}:

$$h_{meas} = \frac{q"}{(T_{s_{meas}} - T_\infty)}. \tag{A.1}$$

The heat flux ($q"$) is determined by dividing the power in by the surface area of the pipe (A_s) as shown:

$$q" = \frac{Q}{A_s}.$$

The pipe surface area is equal to the length of the pipe multiplied by its circumference:

$$q" = \frac{Q}{\pi DL}.$$

Substituting in the values for Q, D, and L, we get:

$$q" = \frac{14.82 \text{ W}}{\pi(0.0159 \text{ m})(0.355 \text{ m})}.$$

Therefore, the heat flux equals:

$$q" = 837.5 \text{ W/m}^2. \quad \text{(A.2)}$$

Substituting in $q"$, $T_{s_{meas}}$, and T_∞ into Equation A.1 we get:

$$h_{meas} = \frac{837.5 \text{ W/m}^2}{(378.07 \text{ K} - 299.15 \text{ K})},$$

Therefore, the measured heat transfer coefficient equals:

$$\boldsymbol{h_{meas} = 10.61 \text{ W/m}^2\text{K}}.$$

Calculating Theoretical Surface Temperature and Heat Transfer Coefficient from Churchill & Chu Correlation:

When determining the theoretical surface temperature ($T_{s_{CC}}$) and heat transfer coefficient (h_{CC}) using the Churchill and Chu correlation, both $T_{s_{CC}}$ and h_{CC} are unknown. As such, an iterative process is often required to determine the true values. In this sample calculation the final iteration is shown using Equations 2.1 through 2.5 and 2.7 presented in Section 2.2 of this thesis.

First, the properties of air are found at $T_\infty = 299.15$ K, from the Air Tables presented in [11] to be:

$\rho = 1.1654 \text{ kg/m}^3$

$\mu = 1.84 \times 10^{-5} \text{ Ns/m}^2$

$v = 1.58 \times 10^{-5} \text{ m}^2/\text{s}$

$k = 2.62 \times 10^{-2} \text{ W/mK}$

$Pr = 0.7072$

The Grashof number (Gr_D) for a circular cylinder is presented in Equation 2.2:

$$Gr_D = \frac{g\beta(T_s - T_\infty)D^3}{v^2}, \quad \text{(2.2)}$$

where β is the volumetric thermal expansion coefficient and is equivalent to the reciprocal of T_∞. T_s is unknown and so is replaced with an estimated value $T_{guess} =$ 113℃ or 386.15K. Additionally substituting in the values for g, β, T_∞, D, and v, we get:

$$Gr_D = \frac{(9.81 \text{ m/s}^2)(0.0033 \text{ } 1/K)(386.15 - 299.15)K(0.0159 \text{ m})^3}{(1.58 \times 10^{-5} \text{ m}^2/\text{s})^2}.$$

Therefore, the Grashof number is:

$$Gr_D = 4.57 \times 10^4 .$$

The Rayleigh number is the product of the Grashof number and Prandtl number and is presented in Equation 2.3:

$$Ra_D = Gr_D \, Pr. \tag{2.3}$$

Substituting in the calculated Grashof and Prandtl numbers we get:

$$Ra_D = (4.57 \times 10^4)\ (0.7072).$$

Therefore, the Rayleigh number is:

$$Ra_D = 3.23 \times 10^4 .$$

This Rayleigh number corresponds to natural convection in a laminar flow regime.

For flows with $Ra_D \leq 10^{12}$ the Churchill and Chu correlation can be used to calculate the theoretical Nusselt number:

$$\overline{Nu_D} = \left\{0.60 + \frac{0.387 Ra_D^{1/6}}{[1 + (0.559/Pr)^{9/16}]^{8/27}}\right\}^2 . \tag{2.5}$$

Substituting in the Rayleigh and Prandtl numbers we get:

$$\overline{Nu_D} = \left\{0.60 + \frac{0.387(3.23 \times 10^4)^{1/6}}{[1 + (0.559/0.7072)^{9/16}]^{8/27}}\right\}^2 .$$

Therefore, the Nusselt number is:

$$\overline{Nu_D} = 5.82.$$

To solve for the theoretical heat transfer coefficient based on the Churchill and Chu correlation (h_{CC}), Equation 2.4 is manipulated to the form:

$$h_{CC} = \frac{\overline{Nu_D} k}{D} . \tag{A.3}$$

Substituting in the Nusselt number, k, and D we get:

$$h_{CC} = \frac{(5.82)(2.62 \times 10^{-2}\ \mathrm{W/mK})}{2.62 \times 10^{-2}\ \mathrm{W/mK}} .$$

Therefore, the heat transfer coefficient based on the Churchill and Chu correlation equals:

$$\boldsymbol{h_{CC} = 9.62\ \mathrm{W/m^2K}}.$$

From here, the theoretical surface temperature ($T_{s_{CC}}$) can be found using Newton's law of cooling:

$$q" = h(T_s - T_\infty), \tag{2.7}$$

by manipulating the equation to:

$$T_{s_{CC}} = \frac{q"}{h_{CC}} + T_\infty. \tag{A.5}$$

Substituting in $q"$ (found in Equation A.2), h_{CC}, and T_∞ we get:

$$T_{s_{CC}} = \frac{837.5\ \mathrm{W/m^2}}{9.62\ \mathrm{W/m^2K}} + 299.15\ \mathrm{K}.$$

Therefore, the theoretical surface temperature based on the Churchill and Chu correlation equals:

$$\boldsymbol{T_{s_{CC}} = 386\mathrm{K}},$$

or

$$\boldsymbol{T_{s_{CC}} = 113}^{\circ}\mathrm{C}.$$

Calculating Theoretical Surface Temperature and Heat Transfer Coefficient from Morgan Correlation:

When determining the theoretical surface temperature (T_{s_M}) and heat transfer coefficient (h_M) using the Morgan correlation, both T_{s_M} and h_M are unknown. As such, an iterative process is often required to determine the true values. In this sample calculation the final iteration is shown using Equations 2.1 through 2.4 and 2.6 through 2.7 presented in Section 2.2 of this thesis.

First, the properties of air are found at $T_\infty = 299.15$ K, from the Air Tables presented in [11] to be:

$\rho = 1.1654\ \mathrm{kg/m^3}$

$\mu = 1.84 \times 10^{-5}\ \mathrm{Ns/m^2}$

$v = 1.58 \times 10^{-5}\ \mathrm{m^2/s}$

$k = 2.62 \times 10^{-2}\ \mathrm{W/mK}$

$Pr = 0.7072$

The Grashof number (Gr_D) for a circular cylinder is presented in Equation 2.2:

$$Gr_D = \frac{g\beta(T_s - T_\infty)D^3}{v^2}, \tag{2.2}$$

where β is the volumetric thermal expansion coefficient and is equivalent to the reciprocal of T_∞. T_s is unknown and so is replaced with an estimated value $T_{guess} =$ 106℃ or 376.15K. Additionally substituting in the values for g, β, T_∞, D, and v, we get:

$$Gr_D = \frac{(9.81\ \mathrm{m}/s^2)(0.0033\ 1/K)(376.45 - 299.15)K(0.0159\ \mathrm{m})^3}{(1.58 \times 10^{-5}\ \mathrm{m^2/s})^2}.$$

Therefore, the Grashof number is:

$$Gr_D = 4.22 \times 10^4\ .$$

The Rayleigh number is the product of the Grashof number and Prandtl number and is presented in Equation 2.3:

$$Ra_D = Gr_D\ Pr. \tag{2.3}$$

Substituting in the calculated Grashof and Prandtl numbers we get:

$$Ra_D = (4.22 \times 10^4)\ (0.7072).$$

Therefore, the Rayleigh number is:

$$Ra_D = 2.98 \times 10^4\ .$$

This Rayleigh number corresponds to natural convection in a laminar flow regime.

For flows with $10^4 < Ra_D < 10^7$ the Morgan's correlation can be used with constants $C = 0.480$ and $n = 0.250$ to calculate the theoretical Nusselt number:

$$\overline{Nu_D} = C\ {Ra_D}^n, \tag{2.6}$$

Substituting in the Rayleigh number and constants $C$and n we get:

$$\overline{Nu_D} = (0.480)(\ 2.98 \times 10^4)^{0.250}.$$

Therefore, the Nusselt number is calculated to be:

$$\overline{Nu_D} = 6.31.$$

To solve for the theoretical heat transfer coefficient based on the Churchill and Chu correlation (h_{CC}), Equation 2.4 is manipulated to the form:

$$h_M = \frac{\overline{Nu_D}k}{D}. \tag{A.6}$$

Substituting in the Nusselt number, k, and D we get:

$$h_M = \frac{(6.31)(2.62 \times 10^{-2}\ \mathrm{W/mK})}{2.62 \times 10^{-2}\ \mathrm{W/mK}}.$$

Therefore, the heat transfer coefficient based on the Churchill and Chu correlation equals:

$$\boldsymbol{h_M = 10.4\ \mathbf{W/m^2K}}.$$

From here, the theoretical surface temperature ($T_{s_{CC}}$) can be found using Newton's law of cooling:

$$q" = h(T_s - T_\infty), \tag{2.7}$$

by manipulating the equation to:

$$T_{s_M} = \frac{q"}{h_M} + T_\infty. \tag{A.7}$$

Substituting in $q"$ (found in Equation A.2), h_{CC}, and T_∞ we get:

$$T_{s_M} = \frac{837.5\ \mathrm{W/m^2}}{10.4\ \mathrm{W/m^2K}} + 299.15\ \mathrm{K}.$$

Therefore, the theoretical surface temperature based on the Churchill and Chu correlation equals:

$$\boldsymbol{T_{s_M} = 379\mathbf{K}},$$

or

$$\boldsymbol{T_{s_M} = 106}\text{℃}.$$

APPENDIX B

Sample Calculation: Particle Displacement under Acoustic Actuation

This appendix presents a sample calculation for determining the particle displacement resulting from an acoustic wave in air. As derived in [19], the magnitude of the particle displacement (ξ) in an acoustic wave depends on the frequency (f) and sound pressure (p_{rms}) of the wave, the density of the air (ρ), and the speed of sound (c_s). Equation B.2 shows the relationship for the particle displacement:

$$\xi = \sqrt{2}\frac{p_{rms}}{2\pi f \rho c_s}. \tag{B.1}$$

From the experimental conditions let the:

Acoustic wave frequency $f = 200$Hz.

Acoustic wave sound pressure level $L_p = 85$ dB.

Reference sound pressure level $p_o = 2 \times 10^{-5}$ Pa.

Air density $\rho = 1.1941$ kg/m^3.

Speed of sound in room temperature air $c_s = 343$ m/s

First, the sound pressure level must be converted from decibels to pascals with the following conversion:

$$L_p = 20log_{10}\left(\frac{p_{rms}}{p_o}\right), \tag{B.2}$$

where L_p is the sound pressure level in dB, p_{rms} is the root mean square pressure in pascals, and p_o is the reference sound pressure in pascals. Manipulating the equation p_{rms} can be solved for:

$$p_{rms} = p_o 10^{L_p/20}.$$

Substituting in the values for L_p and p_o we get:

$$p_{rms} = (2 \times 10^{-5}\text{ Pa})10^{85dB/20},$$

$$p_{rms} = 0.36\ Pa.$$

We can then solve for particle displacement (ξ) by substituting the values for f, p_{rms}, ρ, and c_s into equation B.1:

$$\xi = \sqrt{2}\left(\frac{0.36\ Pa}{2\pi\ (200\text{ Hz})(1.1941\text{ kg/m}^3)(343\text{ m/s})}\right).$$

Therefore, the magnitude of the particle displacement in this acoustic wave is calculated to be:

$$\boldsymbol{\xi = 0.99\ \mu m}.$$